AGU ADVANCING EARTH AND SPACE SCIENCE

JGR Planets

RESEARCH ARTICLE
10.1029/2022JE007223

Key Points:
- We evaluate the contribution of Color and Stereo Surface Imaging System (CaSSIS) color images in the Ladon basin where high-resolution data sets (HiRISE, Context, and Compact Reconnaissance Imaging Spectrometer for Mars [CRISM]) are available
- Data analysis suggests Amazonian ultramafic volcanism and listwanitization in East Ladon
- CaSSIS color images fill the gap between color HiRISE images and CRISM hyperspectral data

Supporting Information:
Supporting Information may be found in the online version of this article.

Author Contributions:
Conceptualization: Daniel Mège, Livio L. Tornabene, Frank Seelos, Francesco Sauro, Ruth Ziethe, Gabriele Cremonese, Nicolas Thomas
Data curation: Daniel Mège

Hydrothermal Alteration of Ultramafic Rocks in Ladon Basin, Mars—Insights From CaSSIS, HiRISE, CRISM, and CTX

Daniel Mège[1], Joanna Gurgurewicz[1], Matteo Massironi[2,3,4], Riccardo Pozzobon[2,4], Gloria Tognon[2], Maurizio Pajola[4], Livio L. Tornabene[5], Alice Lucchetti[4], Beatrice Baschetti[2], Joel M. Davis[6], Ernst Hauber[7], Barbara De Toffoli[6], Sylvain Douté[8], Laszlo Keszthelyi[9], Lucia Marinangeli[10], Jason Perry[11], Antoine Pommerol[12], Loredana Pompilio[10], Angelo Pio Rossi[13], Frank Seelos[14], Francesco Sauro[15], Ruth Ziethe[16], Gabriele Cremonese[4], and Nicolas Thomas[12]

[1]Centrum Badań Kosmicznych Polskiej Akademii Nauk (CBK PAN), Warszawa, Poland, [2]Dipartimento di Geoscienze, Università degli Studi di Padova, Padua, Italy, [3]Centro di Ateneo di Studi e Attività Spaziali, Università degli Studi di Padova, Padua, Italy, [4]INAF-OAPD, Padua, Italy, [5]Department of Earth Sciences, Institute for Earth and Space Exploration, Western University, London, ON, Canada, [6]Natural History Museum, London, UK, [7]Institute für Planetenforschung, DLR, Berlin, Germany, [8]Université Grenoble Alpes, CNRS, CNES, IPAG, Grenoble, France, [9]Astrogeology Science Center, U.S. Geological Survey, Flagstaff, AZ, USA, [10]Università degli Studi G. d'Annunzio, Chieti-Pescara, Italy, [11]University of Arizona, Tucson, AZ, USA, [12]Physikalisches Institut, Universität Bern, Bern, Switzerland, [13]Constructor University, Bremen, Germany, [14]Applied Physics Laboratory, Johns Hopkins University, Laurel, MD, USA, [15]Dipartimento di Scienze Biologiche, Geologiche e Ambientali, Università di Bologna, Bologna, Italy, [16]M&S Software Engineering, Bern, Switzerland

Abstract The evolution of the Ladon basin has been marked by intense geological activity and the discharge of huge volumes of water from the Martian highlands to the lowlands in the late Noachian and Hesperian. We explore the potential of the ExoMars Trace Gas Orbiter/Color and Stereo Surface Imaging System color image data set for geological interpretation and show that it is particularly effective for geologic mapping in combination with other data sets such as HiRISE, Context, and Compact Reconnaissance Imaging Spectrometer for Mars. The study area displays dark lobate flows of upper Hesperian to early Amazonian age, which were likely extruded from a regional extensional fault network. Spectral analysis suggests that these flows and the underlying rocks are ultramafic. Two distinct altered levels are observed below the lobate flows. The upper, yellow-orange level shows hundreds of structurally controlled narrow ridges reminiscent of ridges of listwanite, a suite of silicified, fracture-controlled silica-carbonate rocks derived from an ultramafic source and from serpentine. In addition to serpentinite, the detected mineral assemblages may include chlorite, carbonates, and talc. Kaolin minerals are detected in the lower, white level, which could have formed by groundwater alteration of plagioclase in the volcanic pile. Volcanism, tectonics, hydrothermal activity, and kaolinization are interpreted to be coeval, with hydrothermal activity and kaolinization controlled by the interactions between the aquifer and the hot, ultramafic lobate flows. Following our interpretations, East Ladon may host the first listwanite ridges described on Mars, involving a hydrothermal system rooted in a Hesperian aquifer and affecting ultramafic rocks from a magmatic source yet to be identified.

Plain Language Summary The payload of the ExoMars Trace Gas Orbiter spacecraft includes the Color and Stereo Surface Imaging System (CaSSIS) camera, which retrieved its first Mars images in 2018. Its strength lies in the combination of spatial and spectral resolution with stereo capabilities made possible by a rotating platform. This study investigates the complementarity between the color images of CaSSIS and other data sets from the Mars Reconnaissance Orbiter: the HiRISE camera, the Context camera, and the Compact Reconnaissance Imaging Spectrometer for Mars (CRISM) hyperspectral imager. In this study, we show how CaSSIS readily reveals composition variations at the surface, such as dark flows and light-toned zones in the underlying rocks. Using CRISM and CaSSIS data, their composition can be determined. It is found that the flows are probably volcanic and that the lighter-toned rocks are hydrothermally altered versions of these rocks. This alteration takes the form of listwanite, mineral assemblage found on Earth in mantle rocks transported to the continental surface after subduction, such as the Oman ophiolites. Our findings make the late geologic history of the eastern Ladon basin singularly complex, a unique groundwater-controlled environment conducive to the formation of base and rare metal deposits.

Formal analysis: Daniel Mège, Joanna Gurgurewicz, Matteo Massironi, Riccardo Pozzobon, Gloria Tognon, Maurizio Pajola, Livio L. Tornabene, Alice Lucchetti, Joel M. Davis, Ernst Hauber, Barbara De Toffoli, Sylvain Douté, Jason Perry, Antoine Pommerol, Angelo Pio Rossi, Frank Seelos

Funding acquisition: Daniel Mège, Joanna Gurgurewicz, Matteo Massironi, Livio L. Tornabene, Angelo Pio Rossi, Gabriele Cremonese, Nicolas Thomas

Investigation: Daniel Mège, Joanna Gurgurewicz, Matteo Massironi, Riccardo Pozzobon, Gloria Tognon, Maurizio Pajola, Livio L. Tornabene, Alice Lucchetti, Joel M. Davis, Ernst Hauber, Barbara De Toffoli, Sylvain Douté, Laszlo Keszthelyi, Lucia Marinangeli, Jason Perry, Antoine Pommerol, Angelo Pio Rossi

Methodology: Daniel Mège, Joanna Gurgurewicz, Matteo Massironi, Riccardo Pozzobon, Gloria Tognon, Maurizio Pajola, Livio L. Tornabene, Alice Lucchetti, Joel M. Davis, Ernst Hauber, Barbara De Toffoli, Sylvain Douté, Laszlo Keszthelyi, Lucia Marinangeli, Jason Perry, Antoine Pommerol, Nicolas Thomas

Project Administration: Joanna Gurgurewicz, Matteo Massironi, Nicolas Thomas

Resources: Livio L. Tornabene, Joel M. Davis, Ernst Hauber, Sylvain Douté, Laszlo Keszthelyi, Lucia Marinangeli, Jason Perry, Antoine Pommerol, Angelo Pio Rossi, Frank Seelos, Ruth Ziethe

Software: Livio L. Tornabene, Ernst Hauber, Sylvain Douté, Antoine Pommerol, Frank Seelos, Ruth Ziethe, Gabriele Cremonese

Supervision: Daniel Mège, Joanna Gurgurewicz, Matteo Massironi

Validation: Daniel Mège, Joanna Gurgurewicz, Matteo Massironi, Riccardo Pozzobon, Gloria Tognon, Maurizio Pajola, Ernst Hauber, Sylvain Douté, Laszlo Keszthelyi, Lucia Marinangeli, Jason Perry, Antoine Pommerol, Angelo Pio Rossi, Frank Seelos, Nicolas Thomas

Visualization: Daniel Mège, Riccardo Pozzobon, Gloria Tognon, Maurizio Pajola, Livio L. Tornabene, Alice Lucchetti, Joel M. Davis, Barbara De Toffoli, Frank Seelos

Writing – original draft: Daniel Mège, Joanna Gurgurewicz, Matteo Massironi, Riccardo Pozzobon, Gloria Tognon, Maurizio Pajola, Livio L. Tornabene, Alice Lucchetti, Joel M. Davis, Ernst Hauber, Barbara De Toffoli, Sylvain Douté

Writing – review & editing: Daniel Mège, Joanna Gurgurewicz, Matteo Massironi, Riccardo Pozzobon, Gloria Tognon, Maurizio Pajola, Livio L. Tornabene, Alice Lucchetti, Joel M. Davis, Ernst Hauber, Sylvain Douté, Francesco Sauro

1. Introduction

Similar to Earth (e.g., Catling & Zahnle, 2020), water has been on Mars since the beginning of the planet's history (Carr & Head, 2015). In contrast to Earth, where the fate of water has been controlled by plate amalgamation, recycling and related processes (e.g., Korenaga et al., 2017), the Martian crust may have been the locus of the main water reservoir until the end of the Noachian, exchanging with the glaciated surface (Carr & Head, 2015), before a significant fraction of the existing water moved to the surface, possibly creating a large polar Hesperian ocean (Carr & Head, 2019; Schmidt et al., 2022), now partly back to the aquifers and partly releasing its oxygen (e.g., Lillis et al., 2017) and hydrogen (e.g., Stone et al., 2020) to space. The existence of aquifers is attested by the landforms that result from groundwater release, such as the outflow channels. Most of these flood-carved channels are thought to have formed during the Hesperian by aquifer depressurization (e.g., Marra et al., 2015), with discharges continuing into the early and middle Amazonian (e.g., Rodriguez et al., 2015). This intense hydrological activity may have resulted in the widespread formation or fluvial transportation and resedimentation of smectites (Weitz et al., 2022). Some flooding events are even younger and are associated with the locations of major late Amazonian volcanic activity (Hargitai & Gulick, 2018). Another clue to groundwater activity may be the deformation of floor-fractured craters (FFCs). Although FFCs are also observed on the Moon (e.g., Jozwiak et al., 2014), indicating that water is not strictly necessary, the presence of buried ice (Schumacher & Zegers, 2011) or a water table (Sato et al., 2010) is thought to be a potentially critical factor for FFC formation on Mars. Their frequent association with major discontinuities such as the planetary dichotomy boundary and with chaotic terrains and outflow channels (Bamberg et al., 2014) suggests that groundwater flow may frequently be involved. It has also been suggested that volcanic activity may be the cause; the dichotomy boundary is likely a site of past intense crustal fracturing and magmatic activity (Gurgurewicz et al., 2022), and aquifer pressurization leading to the triggering of outflow channels is more readily achieved when the crust is heated by some underlying magma body. For this reason, similar to the Moon (Jozwiak et al., 2014), magma intrusion and subsequent crater floor uplift might be a cause for FFC formation even in the absence of groundwater or ice (Bamberg et al., 2014). Luzzi et al. (2021) suggested that FFC fracturing could result from a succession of magmatic inflation and deflation episodes.

A number of FFCs are located in the Ladon basin area (Bamberg et al., 2014), indicating that Ladon is a suitable place to investigate floor fracturing, volcanic activity, and groundwater or ground ice. Large volumes of sediments were deposited in the Ladon basin (Figure 1) during the late Noachian and Hesperian periods (Grant & Parker, 2002) and transported from the surrounding Noachian terrains through a vast and multiphase drainage system. Groundwater flow is thought to play an important role in the evolution of the region in connection with the formation of several nearby chaotic terrains. The basin underwent later widespread extensional fracturing and more sparsely, contractional deformation (Irwin & Grant, 2013). This deformation is in the form of wrinkle ridges, that is, a broad ridge with a wrinkle on one side reported forming exclusively in stratified lava flows (Schultz, 2000).

Onboard ESA's ExoMars Trace Gas Orbiter, the Color and Stereo Surface Imaging System (CaSSIS; European Space Agency, 2021) is particularly adapted to geologic mapping due to both its color capabilities and pixel size (4.6 m) imaging capabilities (Thomas et al., 2017, 2022). One of the major characteristic features of the Ladon basin is the polygonal faulting (Irwin & Grant, 2013), leading to the formation of deep troughs that cut the upper stratigraphy of the basin deposits. Several CaSSIS images of the Ladon basin show such fractures and grabens but the regional pattern is best seen in regional mosaics (Figure 2). These sites were targeted to test the spectral capabilities of the four filters of CaSSIS blue-green (BLU), broad red (PAN), and two near-infrared (RED, NIR). In one particular location of the basin (Figure 1c), two overlapping CaSSIS color images were taken (without stereo acquisition) and overlapped four HiRISE images, one CRISM cube, and a Context (CTX) stereo pair. This area in the eastern sector of the Ladon basin has been the main focus of this study.

The area covered by the CaSSIS images is marked by a network of faults, dark lobate units, and light-toned patches. It is surrounded by several FFCs. An interpretation of the fracture pattern and its significance in relation to the broad context of the basin is proposed and a morphological description of the rock units is given, supported by HiRISE images and topographic information. Compositional information is retrieved using both CRISM and CaSSIS data. A detailed mineralogical analysis is conducted at three site of the CRISM cube, including spectral ratioing and band absorption analysis. Spectral cluster analysis applied to CaSSIS images reveal useful details in discriminating between pristine rocks and their alteration products. The interpretations are put into a
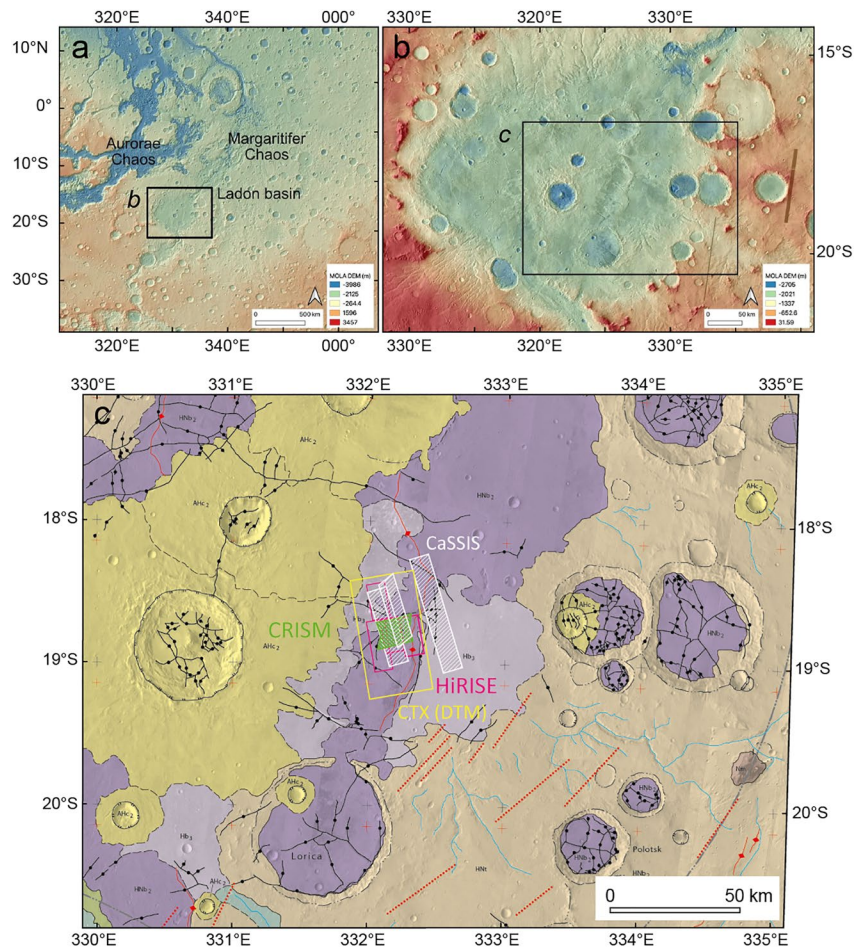
Figure 1. MOLA context of the Ladon basin and the footprints of studied Color and Stereo Surface Imaging System (CaSSIS) images. (a) Panel location of Ladon Basin in the equatorial region of Mars; (b) physiography of Ladon Basin. Basemap is MOLA MEGDR gridded data at 463 m/pixel draped in transparency onto THEMIS infrared (IR) daytime infrared at 100 m/pixel; and (c) footprints of the image data and Compact Reconnaissance Imaging Spectrometer for Mars cube coverage at the study site, in the context of the geologic map by Irwin and Grant (2013). Note the floor-fractured craters distributed around the study site.

chronological perspective with a new crater retention age calculation. Finally, a synthesis is provided in the form of a cross-section representative of the East Ladon site, highlighting the structure, stratigraphy, and alteration systems in the study site.

2. Data Sets and Methods

2.1. CaSSIS Color Composite Mosaic Interpretation and Compositional Analysis

CaSSIS color images have a ground pixel size of ~4.6 m/pixel, with a swath width of 7–9 km and length of 40–50 km. The CaSSIS camera is equipped with four color channels in the blue (BLU), red (PAN), and near-infrared (RED, NIR) ranges (Thomas et al., 2017). The CaSSIS acquisitions can be planned both in stereo configuration and in single acquisition mode, with 1–4 color filters. The vast majority of observations in the Ladon basin so far are single acquisitions with less than four filters, usually 2 or 3. Visualizing the NIR-PAN-BLU and RED-PAN-BLU band combinations as RGB images has proven especially useful to render rock composition contrasts and, for instance, distinguish between pristine bedrock and alteration products.

A survey of polygonal fractures in Ladon basin based on the available CaSSIS images was first carried out (Table 1). We then focused on an area in East Ladon where a mosaic of two CaSSIS images was targeted at a
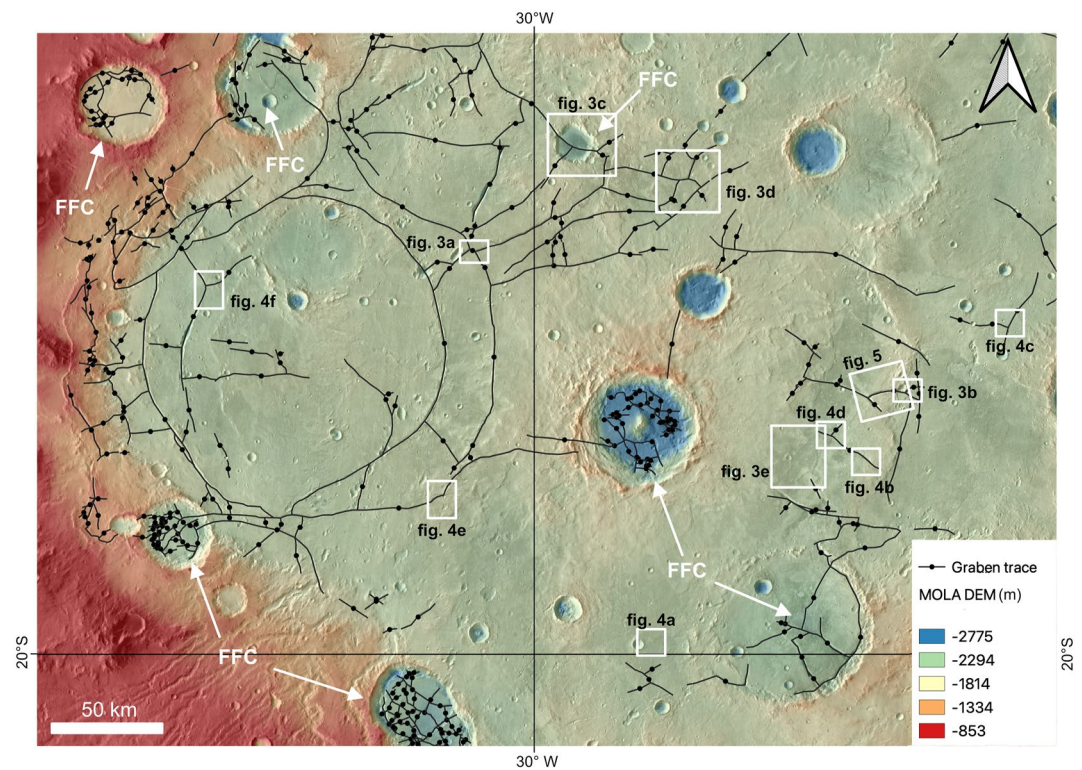
Figure 2. Map of fractures and graben patterns inside the Ladon basin. The floor fractured craters (FFC), characterized by polygonal fractures, are indicated. The white boxes highlight the location of the insets of the Color and Stereo Surface Imaging System images displayed in Figures 3–5. Basemap is the THEMIS IR daytime infrared mosaic at 100 m/pixel colorized with a partially transparent overlay over the MOLA MEGDR gridded data at 463 m/pixel.

location that benefits from excellent CTX, HiRISE, and CRISM coverage (Figure 1c, Table 2), making it possible to optimally investigate the synergy of these data sets.

In East Ladon, CaSSIS images were used qualitatively to identify and map boundaries between geologic terrains. Semiquantitatively, the intensity of alteration can be evaluated using the CaSSIS images through the K-mean spectral clustering technique (Marzo et al., 2006), which makes it possible to find the intrinsic number of clusters characterizing the data set itself, using the Caliński-Harabasz criterion (Caliński & Harabasz, 1974). The resulting clusters are identified by an average spectrum and its associated variability. Since the geographic information is maintained in the process, we can directly compare the spectral clusters with the units and features identified in the geological map. This process has already been applied and tested on various Solar System bodies, such as Mars (Marzo et al., 2006, 2008, 2009), Phobos (Pajola et al., 2018), and Mercury (Lucchetti et al., 2018, 2021; Pajola et al., 2021).

2.2. CTX Images

The broader context is provided by CTX (Malin et al., 2007) panchromatic images at ~6 m/pixel. We generated a controlled CTX mosaic by selecting observations with similar illumination conditions (i.e., incidence angle ~60°). We processed the raw CTX image files from the Planetary Data System (PDS) with the Integrated Software for Imagers and Spectrometers 3 (ISIS3) (Torson & Becker, 1997) and created a network of control points that locate the same morphology or feature in overlapping images. In this way, precise coregistration of images and almost seamless stitching are possible. To refine this product, each CTX image was also equalized with respect to the others to obtain consistent grayscale values throughout the mosaic. Additionally, a blending algorithm with a buffer width of 100 pixels was used to avoid creating seams at the edges of individual images.

Table 1

Color and Stereo Surface Imaging System (CaSSIS) Product IDs Used in This Work and Associated Bandpass Filters (Nominal Band Center/Width From Thomas et al. (2017))

CaSSIS image ID	Channels			
	BLU (497/134 nm)	PAN (677/232 nm)	RED (835/98 nm)	NIR (940/120 nm)
MY35_012254_200_0	X	X	X	X
MY35_010295_341_0	X	X	X	X
MY35_009668_200_0		X		
MY35_009643_200_0		X		
MY35_009581_202_0		X		
MY35_009382_201_0		X		
MY35_007119_203_0	X	X		X
MY35_006970_201_0	X	X		X
MY35_006945_200_0	X	X	X	
MY34_005565_202_0	X	X		X
MY34_004533_198_0	X	X		
MY34_004359_201_0	X	X		X
MY34_004334_200_0	X	X		X
MY34_004272_200_0	X			X
MY34_004247_199_0	X	X		X
MY34_003867_340_0	X	X		X
MY34_003693_342_0	X	X	X	X
MY34_003494_340_1	X	X		X
MY34_003494_340_2	X			X
MY34_002375_340_0			X	X

Note. The available filters (BLU, PAN, RED, and NIR) are checked. The best R-G-B combination, to highlight alteration, basaltic bedrock, and flows was found to be, where available, NIR-PAN-BLU. RED-PAN-BLU yields very similar results.

2.3. CTX Digital Terrain Model Generation and Analysis

We generated a CTX digital terrain model (DTM) using a combination of ISIS3 and the BAE Systems photogrammetric package SOftCopy Exploitation Toolkit (SOCET SET), following the method of Kirk et al. (2008). The CTX DTM was tied to Mars Orbiter Laser Altimeter (MOLA) shot points and exported with a post spacing of 20 m/pixel. The HDEM SfS method (High-resolution Digital Elevation Model from Shape-from-Shading, Douté & Jiang, 2019; Jiang et al., 2017) was applied to the 6 m/pixel ortho-image F20_043532_1613_XN_18S028W adding fine-scale 3D information to the photogrammetrically generated CTX DTM. HDEM SfS takes the DTM

Table 2

Data Used in the East Ladon Site

HiRISE images	CTX images for DTM generation	CaSSIS images	CRISM cube
ESP_064169_1615	F20_043532_1613	MY35_012254_200_0	FRT000128EA[b]
ESP_062745_1615		MY35_006945_200_0[a]	
ESP_043532_1615	B09_013045_1614	MY34_002009_200_0[a]	
ESP_013045_1615			

Note. The three Color and Stereo Surface Imaging System (CaSSIS) images are shown on Figure 5.

[a]The two overlapping CaSSIS images. Compact Reconnaissance Imaging Spectrometer for Mars (CRISM) cube processing is described in Section 1 in Supporting Information S1. [b]In an attempt to complete the observations made with the cube FRT000128EA, the neighboring FRT0001750D cube was investigated as well but its poor signal-to-noise ratio did not make possible to usefully complement the information obtained with the cube FRT000128EA.

and the ortho-image as inputs and iteratively refines the coarse input DTM via the minimization of a total cost function that integrates an intensity model of the image based on a novel radiative transfer scheme and two regularization terms. The image model is built according to the geometrical acquisition conditions of the ortho-image and assuming a homogeneous bidirectional reflectance throughout the scene, taken as the Martian standard photometric function of Vincendon (2013). The HDEM algorithm operates at horizontal scales of meters to hectometers. The vertical relative accuracy has been estimated to be in the order of 1 m, based on the level of morphologic detail achieved and previous numerical tests (Douté & Jiang, 2019).

2.4. HiRISE Image Mosaic Interpretation

A mosaic of four High Resolution Imaging Science Experiment (HiRISE) images (A. S. McEwen et al., 2007), three of which were at a pixel size of 50 cm/pixel and the other at 25 cm/pixel, was produced. It overlaps the two studied CaSSIS images and was used to test and refine interpretations from the more spatially extensive CaSSIS data set. For instance, linear ridges that are not visible at the CaSSIS scale could be identified at the HiRISE scale and interpreted in geological terms.

2.5. CRISM Compositional Analysis

The southern half of the CaSSIS mosaic of the East Ladon site is covered by a CRISM cube (S. Murchie et al., 2007), from which we analyzed the TER and MTRDR products (Seelos, 2016a, 2016b). The CRISM analysis protocol (Section 1 in Supporting Information S1) consists of three steps. In the first step, the spectral parameters defined by Viviano-Beck et al. (2014) were examined in order to get a first idea of the mineralogy within the cube. In the second step, the spectral characteristics which are persistent in the pixels throughout the cube were identified. A dune field that lines the graben visible in the north of the study area was found to be a type-region with a spectral signature representative of the entire scene. In the third step, mineralogical information was retrieved from the identified geologic units and alteration levels. Their averaged spectra were ratioed with the averaged spectrum of the type-region. Mineralogy was interpreted based on the comparison between spectral absorptions and library spectra. The signal-to-noise ratio was additionally improved by mobile averaging of the resulting spectra. Mobile averaging was performed using a long box of 11 channels when seeking mafic minerals in the spectra because mafic minerals show long-wavelength spectral variations. The box included three or seven CRISM channels when seeking alteration minerals, which have much narrower absorption bands.

3. Geological Analysis

3.1. Geological Setting

Geologic mapping of the Ladon Basin by Irwin and Grant (2013) highlighted sedimentary basin fill units of late Noachian to late Hesperian age. In particular, the exposed stratigraphy includes multiple facies and depositional environments interpreted to be composed of coarse flood deposits from Ladon Vallis and finer-grained alluvium from radial valley networks. This unit (HNb2, Figure 1c) might also include minor components of strongly indurated aeolian infilling and volcanic sheets. HNb2 is overlain by a later embayment of volcanic materials or well-indurated sedimentary deposits (Hb3). Finally, superimposed simple and complex craters and their ejecta blankets partly cover the entire basin infilling sequence (AHc2). Apart from some younger impacts, the last phase of geological events involving the most part of the basin is dominated by faulting, predominantly extensional. The selected site in Ladon, however, is located on the nonwrinkled side of a wrinkle ridge formed in unit HNb2.

3.2. Late Polygonal Faults and Ridges in Ladon Basin

Analysis of the CTX mosaic revealed that the main focus of the extensional faulting (excluding FFCs) is located in the western part of the Ladon basin, where a concentric and radial pattern of normal faults is centered roughly between 30°0'W-33°0′W longitude and 16°20′–19°20′S latitude (Figure 2). Grabens radiate from this area to almost the entire basin floor, reaching the eastern margin where they appear more sporadically.

All over the basin, grabens show T- and Y-shaped junctions (Figures 3 and 4), defining polygonal faulting, which according to recent studies on Earth sedimentary basins (Collanega et al., 2020), are expressions of a radial
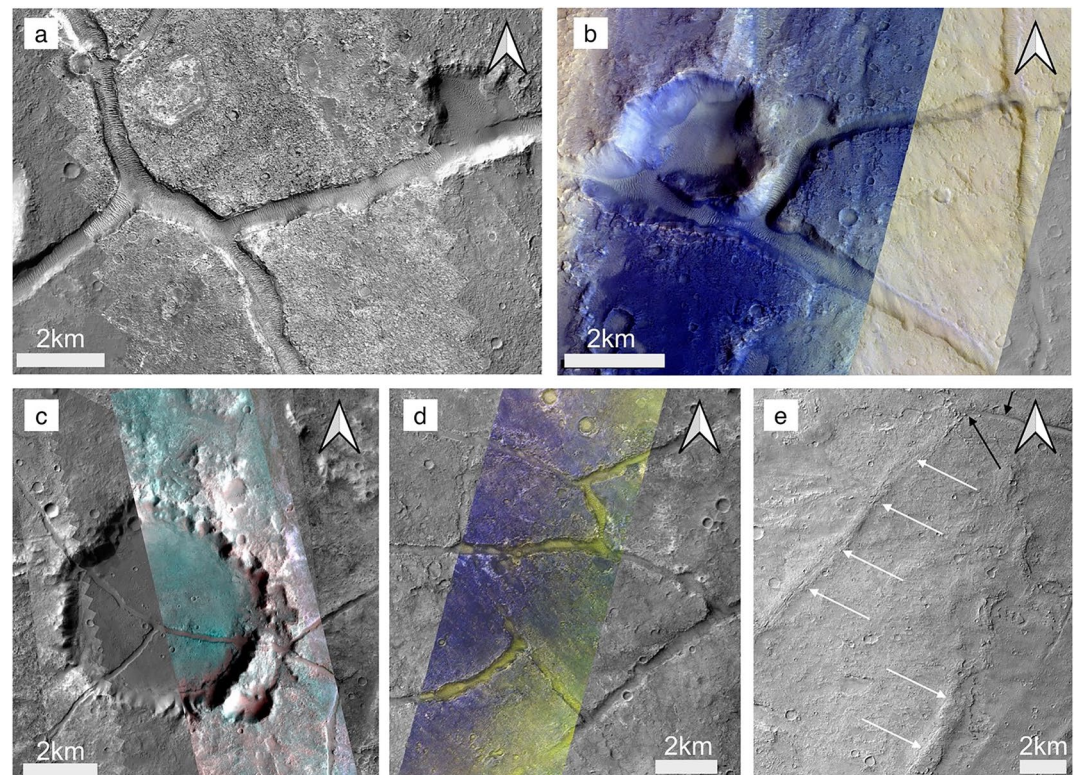
Figure 3. Color and Stereo Surface Imaging System (CaSSIS) and Context Camera (CTX) images showing T- and Y-shaped grabens. Locations are in Figure 2 and image numbers are in Table 1. Panels (a–d) show CaSSIS images overlying the Murray Lab CTX mosaic (Dickson et al., 2018). The CaSSIS IDs are (a) MY35_009668_200_0 (PAN); (b) overlay of MY34_003867_340_0 (BLU-PAN-NIR) and MY34_003494_340_2 (BLU and NIR); (c) overlay of MY34_004533_198_1 (BLU and PAN) and MY35_009382_201 (PAN); and (d) MY34_003693_342_1 (NIR-PAN-BLU). Panel (e) shows two ridges (white arrows), one of which transitions to a graben (black arrows). Murray Lab CTX mosaic centered at 18.7°N, 331.8°E.

extension. In few cases, grabens crosscut the rim of FFCs, where the deformation is even more pervasive. This suggests a causative relationship between the regional radial stress and the FFC, where the oblate extensional deformation could have developed more easily, favored by the inherited impact fracturing and damage.

Several grabens gradually become positive ridges along the strike (Figure 3e). This observation excludes any kind of regional compressional reactivation since it would have caused the inversion of the related grabens along their entire length, as well as compressional reactivation of all the extensional features in proximity having a similar orientation. Thus, the most obvious interpretation for these linear ridges is that they are dikes that are more resistant to erosion than their host rock. The grabens are also intimately associated with dark lobate deposits and, locally, with white and yellow-orange alteration patches (Figure 4) as characterized at the study site in East Ladon (Figure 5).

The CaSSIS images (Table 1) at the East Ladon study area (Figure 5) are of particular geologic interest, in addition to benefitting from a rich data set coverage (Figure 1c). Located between FFCs, they display grabens with a Y-shaped junction, dark lobate deposits, alteration patches and small aligned ridges. Detailed geological mapping of these images together with a three-dimensional analysis of HiRISE data and a compositional study using the CRISM data are reported in the following sections (Sections 3.3, 3.4 and 4).

3.3. Geological Units on CaSSIS Images in the East Ladon Study Area

The analyses of the CaSSIS NIR-PAN-BLU color composite of the East Ladon study area allowed us to identify three main geological units in the bedrock (Figure 6). Geological mapping shows local complexity, which is not evident on the much broader geological map of Irwin and Grant (2013) (Figure 1c). Stratigraphically, from
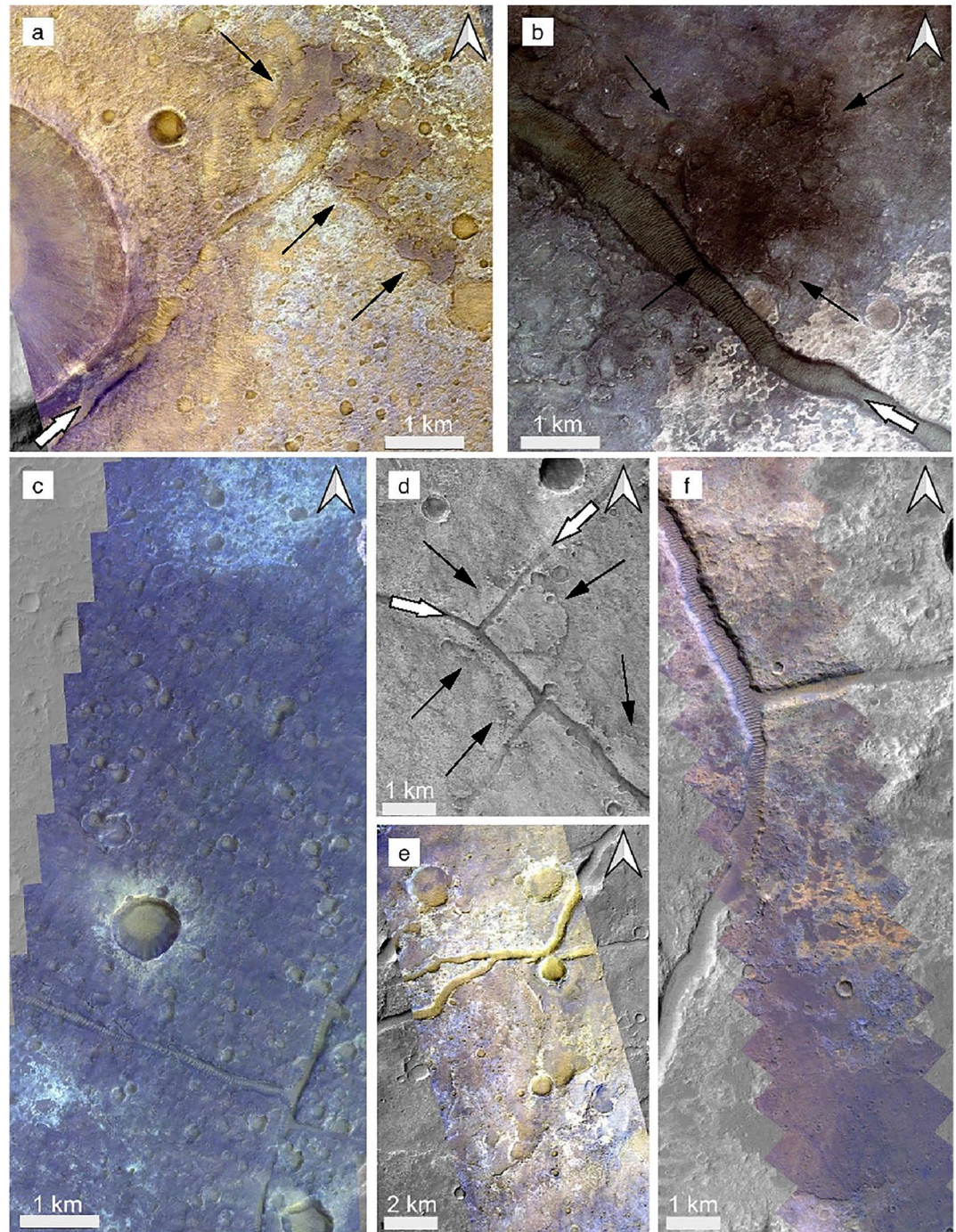
Figure 4. Color and Stereo Surface Imaging System (CaSSIS) and Context Camera (CTX) Images showing flow fronts and/or alteration patches. Locations are in Figure 2 and image numbers are in Table 1. Black arrows point to flow features akin to Unit 3 in the East Ladon study site (Figure 6), and white arrows point to the associated graben. The CaSSIS IDs are (a) MY34_005565_202_0 (NIR-PAN-BLU); (b) MY34_002375_340_0 (RED and NIR); (c) MY35_010295_341_0 (NIR-PAN-BLU); (d) CTX image P11_005503_1637_XN_16S028W; (e) MY34_004359_201_0 (NIR, PAN, and BLU); and (f) MY35_006970_201_0 (NIR-PAN-BLU).

bottom to top, the following units are recognized (Figure 6): (a) a rough and bluish Unit 1, locally changing to white and yellow-orange patches; (b) a smoother Unit 2 of bluish resistant material with locally yellow-orange patches; (c) a dark blue-violet (indigo), smooth capping unit closely associated with the grabens (Unit 3). On the plateau surface, each unit is separated by the others by a scarp usually 10–30 m high. The grabens are NW and
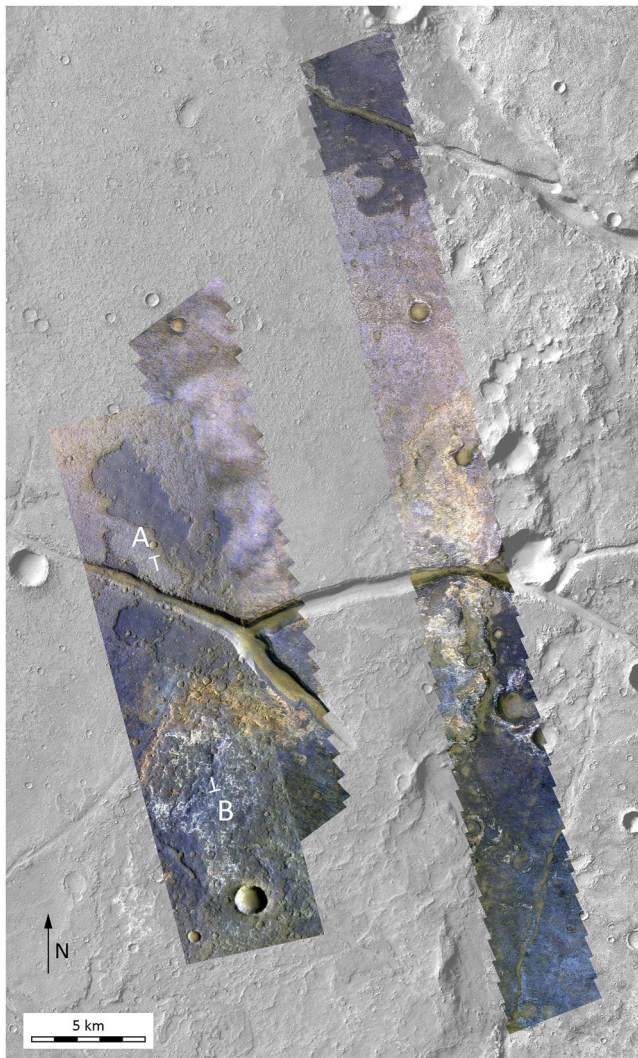
NE oriented, they show a Y-shaped junction and act as sand traps (Figures 5 and 6).

Units 1 and 2 correspond to HNb2 and Hb3 in the Irwin and Grant's (2013) geologic map, respectively, but Unit 3 is not defined. It stratigraphically overlies Unit 2 and where Unit 2 is eroded away, it overlies Unit 1. Unit 3 is composed of several distinct sheets bounded by lobate fronts that sometimes overlap each other. These features suggest a flow origin, whether lava or mud (Brož et al., 2020). CTX images reveal that similar flows are widespread throughout the Ladon basin and are associated with grabens and ridges (Figures 4a, 4b and 4d). Although the graben formation is usually the youngest identified geological event in the basin evolution, units akin to Unit 3 and the associated grabens do not always show unequivocal crosscutting relationships. In most, though not all cases, the flows are observed to be cut by the graben fault scarps, suggesting that flows are precursor events to the surface fracturing.

3.4. Alteration Levels on CaSSIS and HiRISE Images

The white and yellow-orange patches observed in Units 1 and 2 on the analyzed CaSSIS images (Figures 5 and 7) may be representative of either stratigraphic unit or altered levels. They are well exposed along the walls of the graben (Figure 8), where they are clearly seen to vary in depth and thickness at the scale of meters, suggesting that they are altered levels rather than part of the original stratigraphy within Units 1 and 2, which appear to be more constant in elevation and thickness. The yellow-orange level is exposed above the white level, over a thickness of 10–40 m on the side of the graben, which is almost 10 times the thickness of the white level. Both levels are usually separated by dark rock. However, HiRISE images suggest that they are locally in contact. In the map view, the white patches are scattered in Unit 1, whereas the yellow-orange patches also appear in Unit 2 when the surface is slightly eroded.

Hundreds of linear ridge of maximum length hundreds of meters are observed (Figure 9). The two overlapping CaSSIS images are also overlapped by HiRISE images (Figure 1c) and the CTX-based DTM, making it possible to correlate observations at different scales with good topographic control. At the HiRISE scale, the yellow alteration level is seen as topographic ridges surrounded by yellow-orange deposits. Ridge height (Figures 9b and 9c) is up to 15 m. The yellow-orange deposits may be debris slopes on the ridge

Figure 5. Color and Stereo Surface Imaging System mosaic (NIR-PAN-BLU) of the East Ladon study site with a magnification of the alteration zones and Y-shaped graben pattern. A and B locate the two endpoints of the geologic section shown in Figure 25. Image IDs are in Table 1.

sides, or, since the yellow-orange terrain is observed to form a continuous layer on the graben walls, an eroded layer abutting against stronger ridges of similar composition. Figure 7d shows that the ridges, when sufficiently exposed, are fully brecciated.

Many ridges follow a common ENE trend (Figure 9a, inset), indicating structural control. The structural trend corresponds to the northeastern segment of the Y-shaped graben. A few ridges correspond to impact crater rims, indicating that rim structures may have acted as alteration pathways. These observations suggest that the alteration is the result of fluids flowing along hydrothermal conduits. Ridge topography indicates that the ridges are more resistant than the surroundings. The white patches appear rather flat and sometimes fracture into meter-to-decameter-scale plates. Their trend is not indicative of structural control.

The DTM indicates that the width of the ridges, debris slopes excluded, does not exceed a few meters. On HiRISE images, many of them are detected at the pixel size resolution, indicating that they are probably much thinner (Mège & Korme, 2004), perhaps even thinner than the 25–50 cm pixel width. Linear ridges in geology include schistosity plane traces, glacial lineations, and veins and dykes. The first two are discarded on the basis of the known geologic environment. Although the definition of a vein, whether igneous or mineral, does not usually
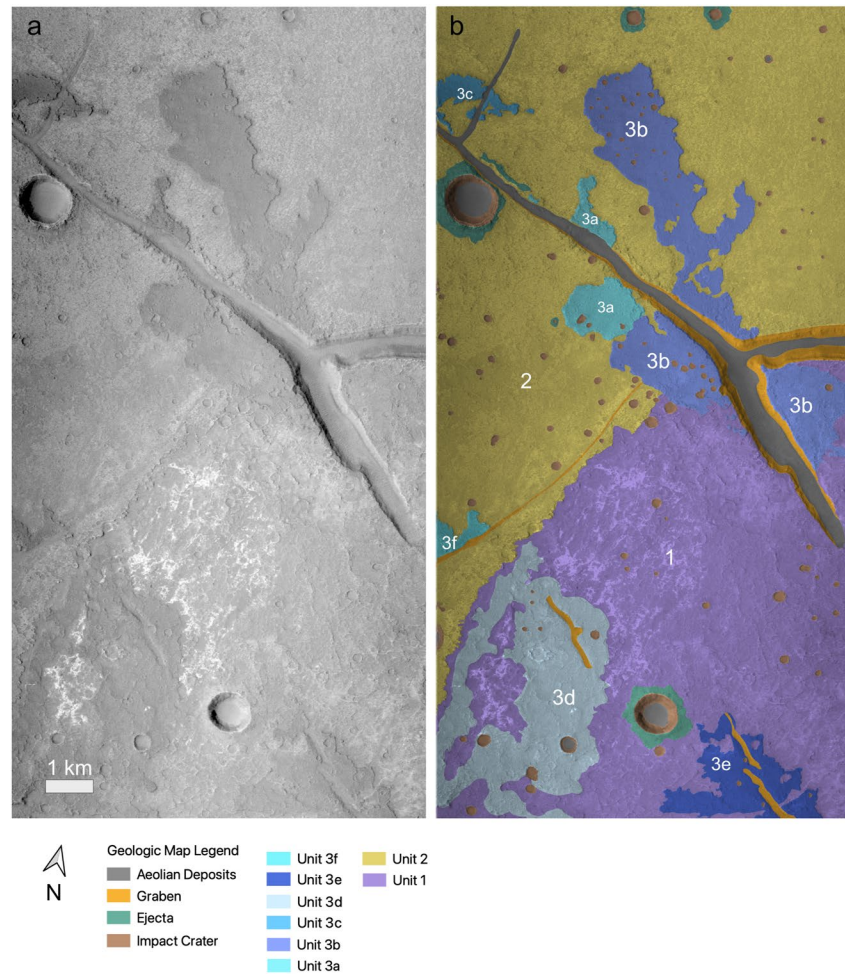
Figure 6. (a) Context Camera (CTX) ortho-image (B09_013045_1614, 6 m/pixel) used for geologic mapping of the East Ladon study site and (b) geological map. Unit numbers increase inversely to their relative age; letters indicate distinct outcrops for the same unit.

include size constraints, vein length and width do not usually exceed meters and centimeters, respectively, and their propagation is sensitive to the stress field in their local environment as well as host rock existing discontinuities, making them usually not strait (e.g., Gudmundsson et al., 2002). Dikes are in better agreement with observations with respect to dimensions, thickness, and straightness. Nevertheless, the restriction to an altered level does not argue in favor of this interpretation. The fully brecciated structure is not typical of magmatic dykes either, even though brecciation is not uncommon in magmatic dikes on Earth. Brecciation does not affect the presence of chilled dike margins or the usual dyke fracturing pattern perpendicular to strike, and such patterns can be seen on HiRISE images (Mège & Gurgurewicz, 2016). Therefore, the nature of these structurally guided linear ridges needs more investigation.

The other CaSSIS image at the Ladon site is not covered by HiRISE imagery or the CTX-based DTM (Figure 1c). The observed geological units are similar to those identified in Figure 6, and similarly, linear ridges are observed in Unit 1 and in the partly eroded Unit 2 (Figure 9d). The ability to map narrow geologic patterns using CaSSIS color imagery in the absence of higher resolution data can therefore be evaluated. The yellow-orange color of the ridges on the CaSSIS image, combined with the shades apparent on panchromatic images of similar resolution (CTX), proves helpful for mapping, although obviously, the lack of HiRISE data limits accuracy. The azimuth-frequency plot (Figure 9d, inset) shows that the ridge orientation, $77.9° \pm 23.11$ (1σ), is similar to that measured on the two overlapping CaSSIS images on Figure 9a, $69.1° \pm 20.32$ (1σ). The ridges seen in Figure 9d
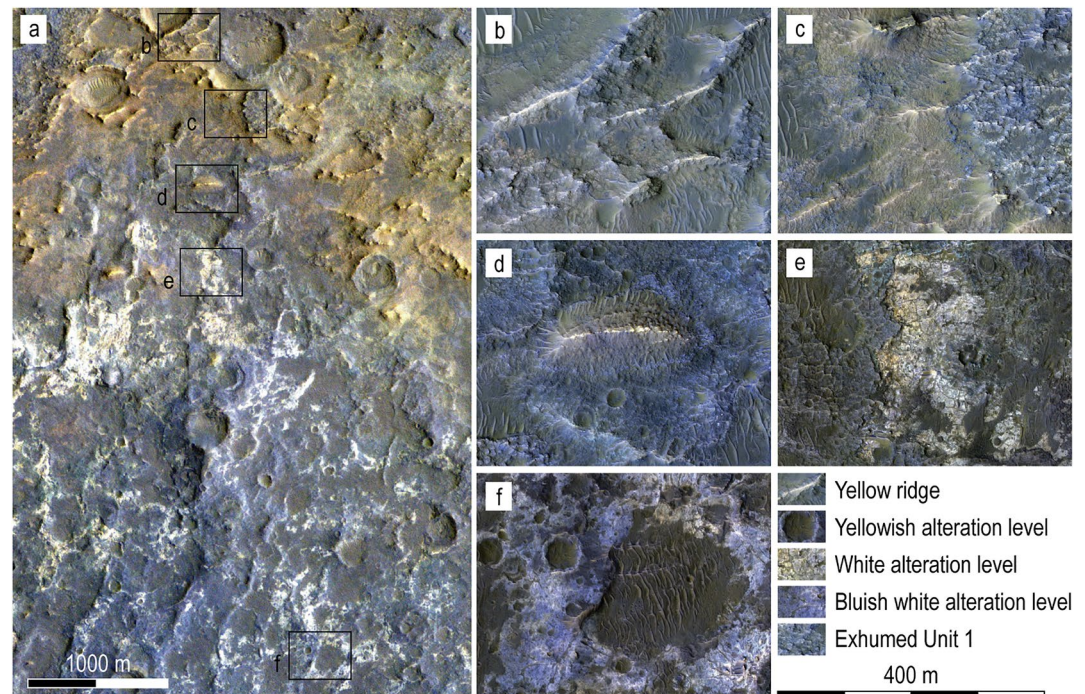
Figure 7. Correspondence between the main discussed geologic units on CaSSIS (CaSSIS image MY34_002009_200_0, bands RED-PAN-BLU as RGB) and one of the HiRISE images (ESP_013045_1615, color).

are located on both sides of the northeastern segment of the Y-shaped graben, suggesting that the stress field that prevailed during their emplacement was similar to that which guided graben formation.

Ridge analysis reveals that the combination of CaSSIS and HiRISE data reduces the likelihood of erroneous interpretations that would result from HiRISE analysis alone. The thickest dikes and veins are so thin that they can be confidently traced along the HiRISE color strip only. Combining the HiRISE resolution and the CaSSIS colors makes it possible to substantially enhance the geologic return both by extending reliable observations throughout the surface area where joint HiRISE and CaSSIS data are available and by highlighting the continuity of structures at the regional scale, as is well known by cartographers working on multiresolution remote sensing data sets. When HiRISE data are not available, the nearly complete CTX coverage of the planet, with a resolution equal to the resolution of the CaSSIS images, is equally helpful for geological interpretation through shades, even without exploiting them by photoclinometry.

4. Composition of Flows and Hydrothermal Alteration Zones

4.1. *K*-Mean Spectral Clustering Technique

We applied the clustering technique to three 100×100 pixels yellow-orange alteration zones. The resulting natural number of clusters for selection 1 (Sel 1), 2 (Sel 2), and 3 (Sel 3) are 3, 6, and 5, respectively. In the three areas, the results spectrally separate the most altered classes along the rectilinear ridges (Figure 10). To highlight the different absorption strengths observable from the ferrous (Fe^{2+}) or ferric (Fe^{3+}) iron spectra, we normalized all spectra at 0.677 μm (band 2). In this way, it is possible to highlight the inverse relationship between the behaviors of bands 3, 4, and band 1. In general, deeper absorption at band 4 equates to a shallower absorption at band 1 and it appears to be sensitive to the presence of ferrous (or mafic) compositions, while the opposite is true for ferric altered compositions. As can be seen from Figure 10, cluster 2 of Sel 1, cluster 5 of Sel 2, and cluster 4 of Sel 3 are well correlated with alteration zones within the graben and imply a ferric composition. The distribution of all the other clusters shows a spreading of the alteration from these ridges outwards. These patterns support an alteration system controlled by strengthened fractures affecting a significantly less weathered bedrock.
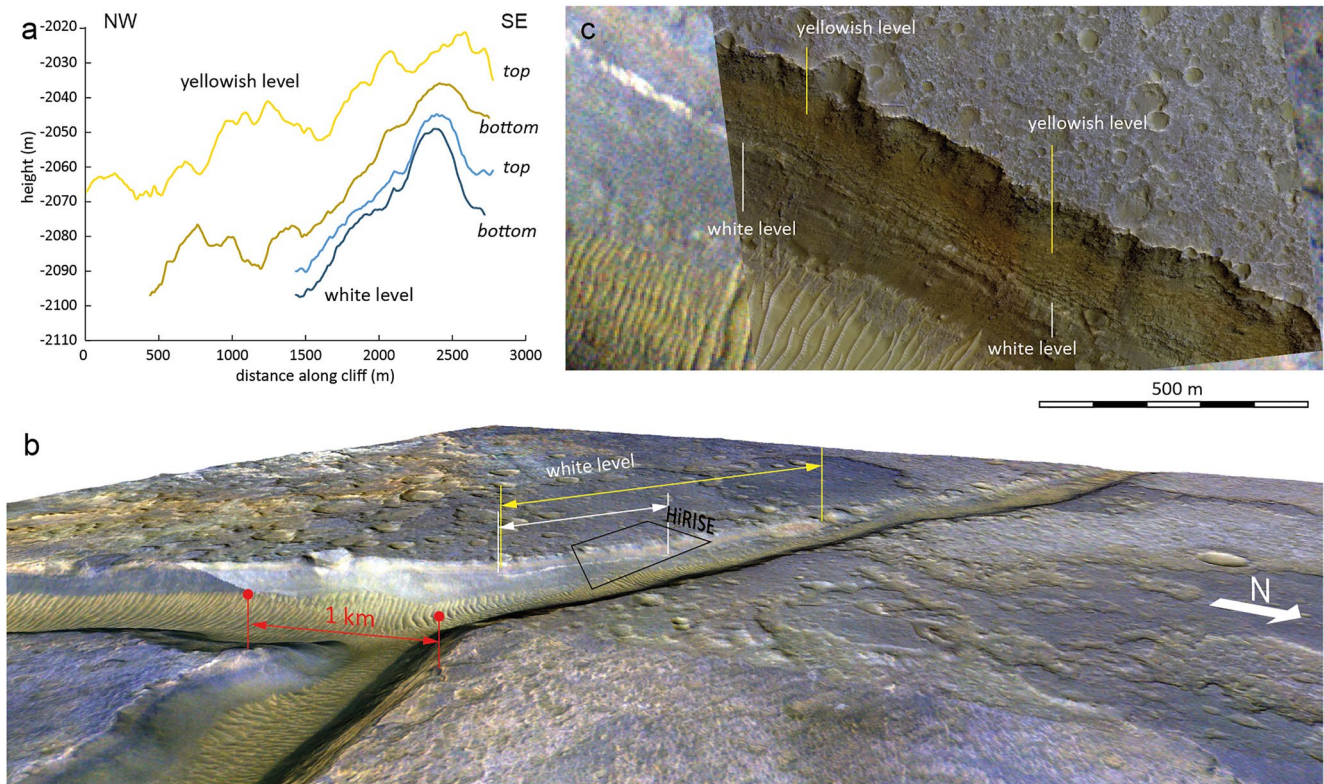
Figure 8. (a) Topographic profiles of the lower and upper contacts between the yellow-orange and white levels and the dark host rock; three-dimensional Color and Stereo Surface Imaging System (CaSSIS) (b) and vertical HiRISE (c) views of the East Ladon study site (no vertical exaggeration). Topographic information was extracted from CTX-derived digital terrain model. The variations in elevation of the yellow-orange and white levels in panel (a) suggest that they are altered levels rather than stratigraphic levels. The lateral extent of the topographic profiles is indicated in panel (b). In panel (b), the CaSSIS image is MY34_002009_200_0 and the RGB composite was obtained using the filters RED, PAN, and BLU, respectively. The HiRISE image in panel (c) is ESP_013045_1615 and the view is located in panel (b).

4.2. Results From Spectral Parameters

Spectral parameters calculated from the CRISM cube are used to guide mineralogical investigations further (Table 3). All the parameters and MTRDR browse products introduced by Viviano-Beck et al. (2014) and refined by Seelos (2016a, 2016b) were reviewed. Those yielding the most significant information were updated using the latest MTRDR versions and are shown in Figures 11 and 12. The FM2 composite shows that nanophase ferric oxides (in red on Figure 11b) are pervasive at the surface. Olivine is well detected in the yellow-orange areas (red on Figure 11c), in contrary to pyroxene. Since these areas are flow alteration products, the flows are interpreted to be of volcanic origin. Olivine is also detected in the flows but is more patchy, probably due to blanketing by the ferric oxides. The better detection of olivine in alteration products than in the flows themselves is interpreted as a consequence of the ridged topography of the yellow-orange level, which should make it less dusty than the horizontal flow surface.

The magenta color of the CAR composite (Figure 12a) suggests that the yellow-orange areas are rich in Fe/Mg phyllosilicates. Their cyan color in the PFM composite indicates either Mg-carbonates or Fe/Mg smectites (Figure 12b). Their blue color on the HYD composite indicates that they include hydrated minerals, though not hydrated sulfates (Figure 12c). The BD3000 parameter shows enrichment in adsorbed or bound water both in the yellow-orange and white areas (Figure 12d). The white areas are often mantled by bluish, likely mafic, minerals (Figure 7f), probably coming from the surrounding flows, in which water is not detected. The detected water is therefore probably a component of the white rock.

The parameters suggest that the study area includes mafic or ultramafic volcanic rocks (Units 1–3) with removal of pyroxenes and addition of phyllosilicates in the yellow-orange terrain of Unit 1. Hydroxylated minerals are present in the yellow-orange terrain, including silicates but perhaps also other mineral families, and water-bearing
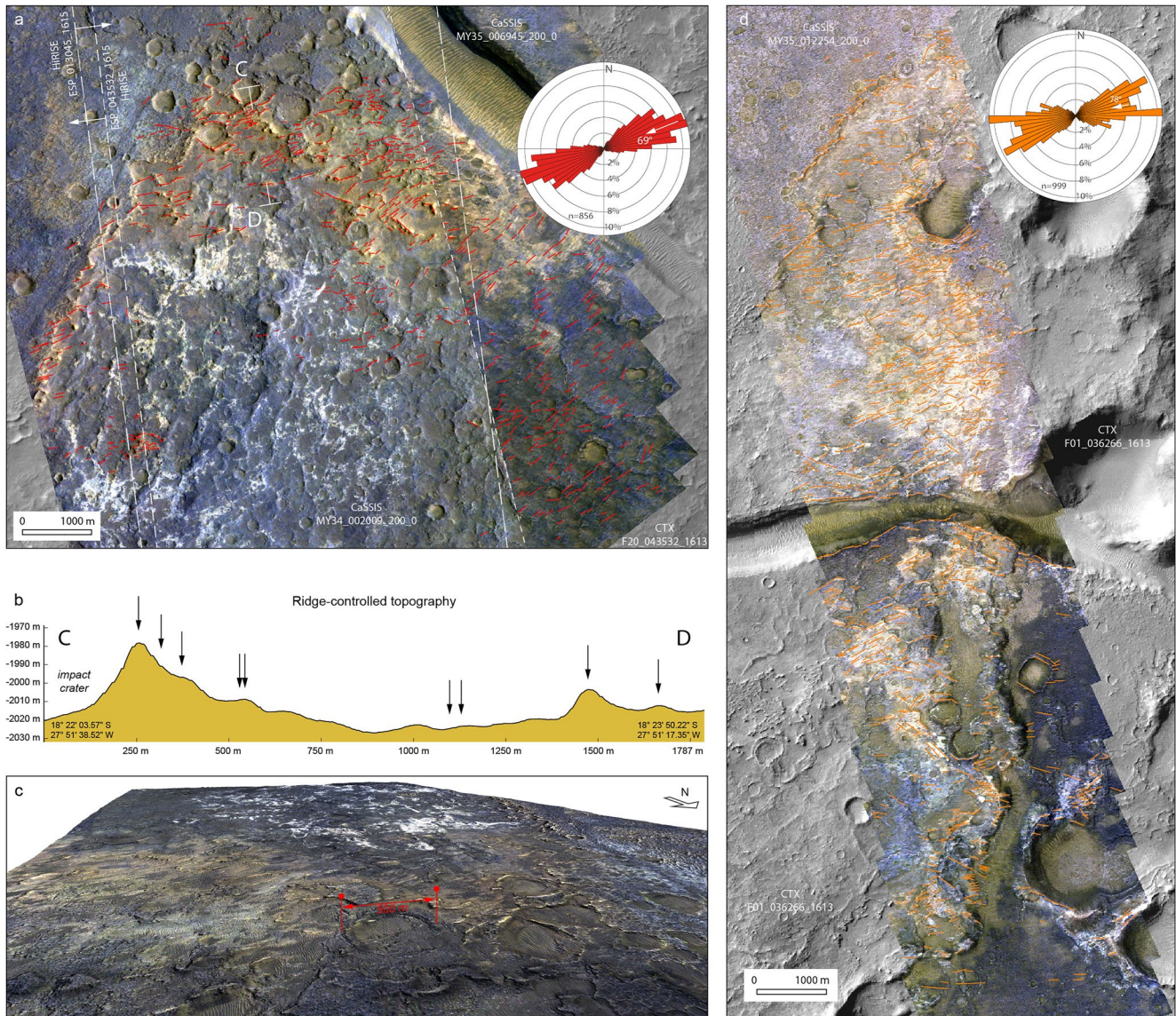
Figure 9. (a) Linear ridges (red) mapped using Color and Stereo Surface Imaging System (CaSSIS) (NIR-PAN-BLU composite) and HiRISE images. The frequency-azimuth plot in the upper right shows a ridge orientation. The short-dashed line locates the boundary between the two images in the CaSSIS mosaic. Lines with longer dashes locate the boundary of the two HiRISE images. (b) Topographic profile across some of the ridges. The arrows mark the inferred positions of the ridges. Topography is from the Context (CTX) digital terrain model generated using the High-resolution Digital Elevation Model from Shape-from-Shading method. Vertical exaggeration is 5×. (c) Perspective view. The ridges are yellow-orange. (d) Linear ridges (orange) mapped using CaSSIS (NIR-PAN-BLUE composite) and CTX images, without the help of HiRISE. The frequency-azimuth plot in the upper right shows a ridge orientation. On the rose diagrams, "n" is the number of measurements.

minerals are expected in the yellow-orange and white terrains. Based on the spectral parameters, sulfates are precluded.

4.3. Analysis of CRISM Spectral Characteristics: Mafic Minerals

Spectra representative of the three flow units (Figure 13) do not show any substantial difference (Figure 14). A broad ~2 µm absorption appears to be present throughout the cube, implying a mafic component consistent with pyroxene-bearing materials. In spite of instrumental artifact, the CRISM spectra also show a deep absorption at ~1 µm and broader absorption between 2.0 and 2.3 µm, consistent with pyroxenes.

Figure 10. The selection of the areas on the Color and Stereo Surface Imaging System data set where the *k*-mean algorithm has been applied. The number of clusters identified are 3, 6, and 5 for selection 1, 2, and 3, respectively (b–d). The average spectra normalized at a value of 1.0 at 0.677 μm are reported f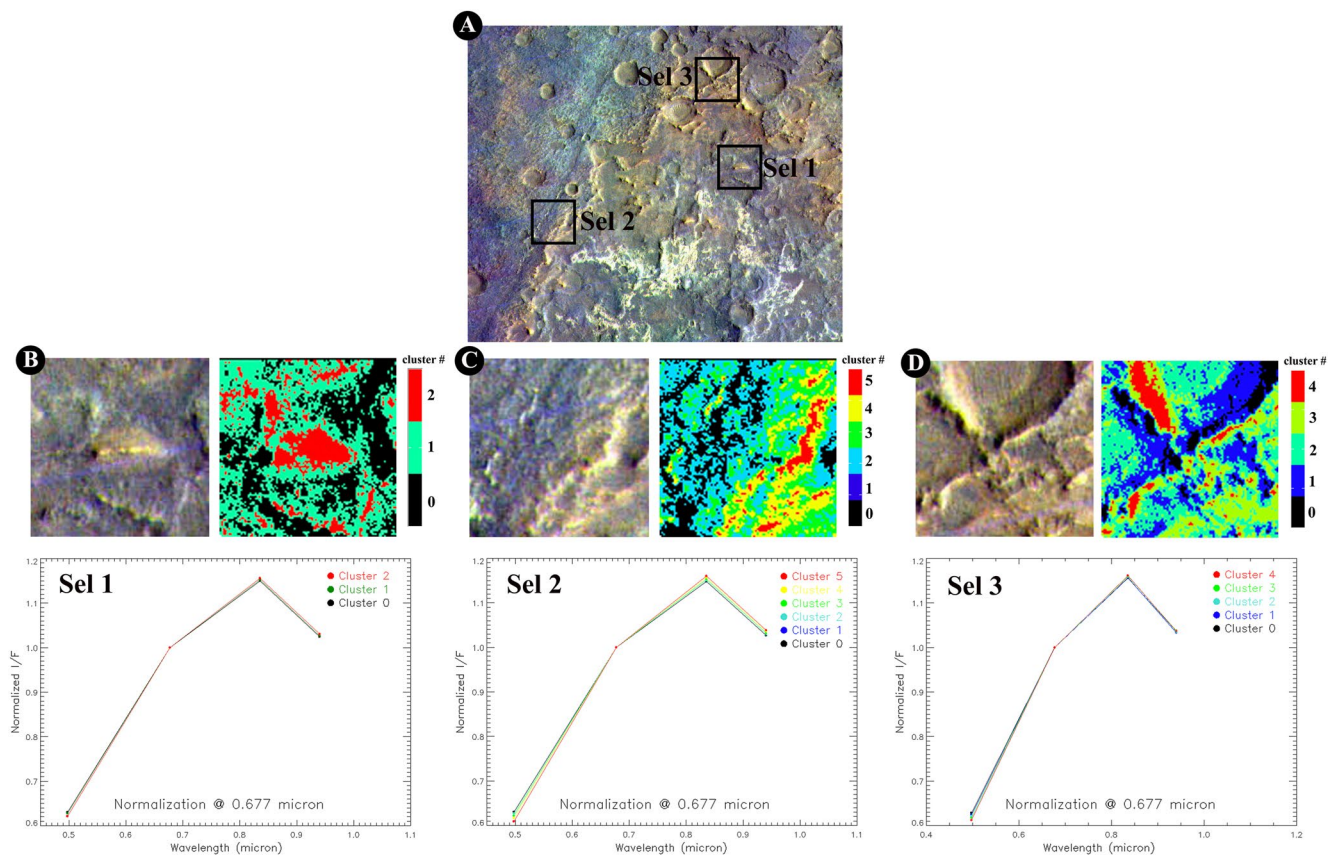or each selection. The colors of the spectra refer to the upper right image of panels (b–d). In all selections, the dikes and veins are identified by the red color cluster.

Olivine also has a major band center at ∼1.05–1.09 μm, which may be covered by the CRISM artifact zone. However, from ∼1 μm toward longer wavelengths, olivine library spectra display a spectral bend which is also found in the CRISM pixels U1-3. The type of olivine, ferrous or Mg-rich, cannot be determined.

4.4. Alteration Minerals

Figure 13 also shows a region of interest (ROI) of 3,969 pixels selected in the dune field located on the floor of the graben visible on the CRISM image. Comparison with the dark terrain samples U1-3 (Figure 14) shows that the dunes are made of the same material. Further, ratioing U1-3 with the averaged spectrum of this ROI (provided in Figure S1 in Supporting Information S1) removes all absorptions (Figure 15). The ROI can therefore be used as a denominator for ratioing spectra from the yellow-orange and white terrains to identify minerals having narrow absorption bands, keeping in mind that olivine and pyroxene are also present but removed by the ratioing. This approach is different from the usual approach, where ratioing is done with bland terrain, absent in this cube. Ratioing makes it possible to remove the long wavelength signature of mafic minerals (Figure 14) while keeping the narrower absorptions of alteration minerals.

The yellow-orange terrain spectra which are the most different from the denominator are located in two ROIs, which correspond Sites A and B on Figure 13. A third ROI, which corresponds to Site C, is representative of the white terrain (see the pixel coordinates in Section 3 in Supporting Information S1).

In Figure 16, the spectrum at Site A is compared with library spectra of serpentinite: antigorite, chrysotile, and lizardite. The three share the same chemical formula but differ in structure. In the CRISM range, the three minerals are characterized by four absorption bands at 1.38–1.41, ∼2, 2.32–2.34, and 2.52 μm, which altogether are diagnostic (Bishop, Lane, et al., 2008; Ehlmann et al., 2010; Viviano-Beck et al., 2014). Moreover, the

Table 3
Mineralogical Interpretation of the Spectral Parameters Used in This Work (After Seelos (2016b)

Color composite	Spectral parameters	Interpretation		
		Flow units	Yellow-orange terrain	White terrain on flow unit
TRU	R600			
True color	R530			
	R440			
FM2	BD530_2	Nanophase ferric oxides	Nanophase ferric oxides	Nanophase ferric oxides
Fe minerals	BD920_2			
	BDI1000VIS			
MAF	OLINDEX3	Olivine	Olivine	Olivine
Mafic minerals	LCPINDEX2	Low-Ca pyroxene	Masked by alteration minerals	Low-Ca pyroxene
	HCPINDEX2	High-Ca pyroxene		High-Ca pyroxene
CAR	D2300		Fe/Mg phyllosilicates (Red, magenta: Fe/Mg phyllosilicates)	
Carbonates	BD2500_2			
	BD1900_2			
PFM	BD2355		Mg Carbonates (Cyan: Mg carbonates or Fe/Mg smectites)	
Phyllosilicates with Fe and Mg	D2300			
	BD2290			
HYD	SINDEX2		Hydrated minerals but not sulfates (hydromagnesite?)	
Hydrated minerals	BD2100_2			
	BD1900_2			
–	BD3000		Adsorbed and bound water (hydromagnesite?)	Adsorbed and bound water in white terrain (alunite?)

spectrum of Site A and the type serpentine from the Minerals Identified through CRISM Analysis (MICA) library (Viviano-Beck et al., 2014) are similar. The similarity is especially strong at wavelengths longer than 1.6 μm. The vibration observed at 1.41 μm at Site A is between the Mg_3-OH overtone at 1.38–1.39 μm and the 1.43 Fe_2-OH overtone (Bishop, Lane, et al., 2008), suggesting an intermediate, (Fe, Mg) serpentine composition. Fifth absorption, at 2.09 μm, is also observed in the MICA type serpentine, and corresponds to an additional band observed between spectral peaks at 2.06 and 2.18 μm in the laboratory serpentine spectra.

Although antigorite forms at higher temperatures than chrysotile and lizardite (Wenner & Taylor, 1971), potentially constraining the formation environment, their difference in near-infrared spectra observed under laboratory conditions (for instance in the 1.4 μm region, King & Clark, 1989) makes them unlikely to be distinguished on the CRISM whole rock measurements. Nevertheless, the mechanical strength of chrysotile is much lower than the strength of antigorite and lizardite (Moore et al., 1996), which suggests that the yellow-orange linear ridges (Figures 7 and 9) dominantly include antigorite and/or lizardite.

Minerals from the chlorite group are frequently associated with serpentinite, and although their reflectance spectra share many absorptions in the CRISM-relevant spectral range, a diagnostic difference exists around 2.3 μm (Bishop, Lane, et al., 2008). Chamosite, the Fe^{2+} end-member of the chlorite group Fe-Mg solid solution, has two strong absorptions, at 2.26 and 2.36 μm (Figure 17). They are not identified at Site A. On the contrary, the Mg^{3+} end-member clinochlore has the same ~2.32 μm band (here at 2.33 μm) as serpentine, but also two shoulders, resulting in a broader, flared band. The spectral shape of Site A does show such a broad band, perhaps more consistent with chlorite than serpentine. A second clue to the presence of clinochlore is its absorption at 2.58 μm, which echoes the 2.59 μm band at Site A, and is not found in the serpentine.

Spectral absorption analysis suggests that due to the presence of diagnostic bands both serpentine and chlorite are present in the CRISM spectra. The 2.09 μm band at sites A and B, although not diagnostic of serpentine (Bishop, Lane, et al., 2008), is present in some terrestrial serpentines (Figure 16) but not in chlorite. In the contrary, the
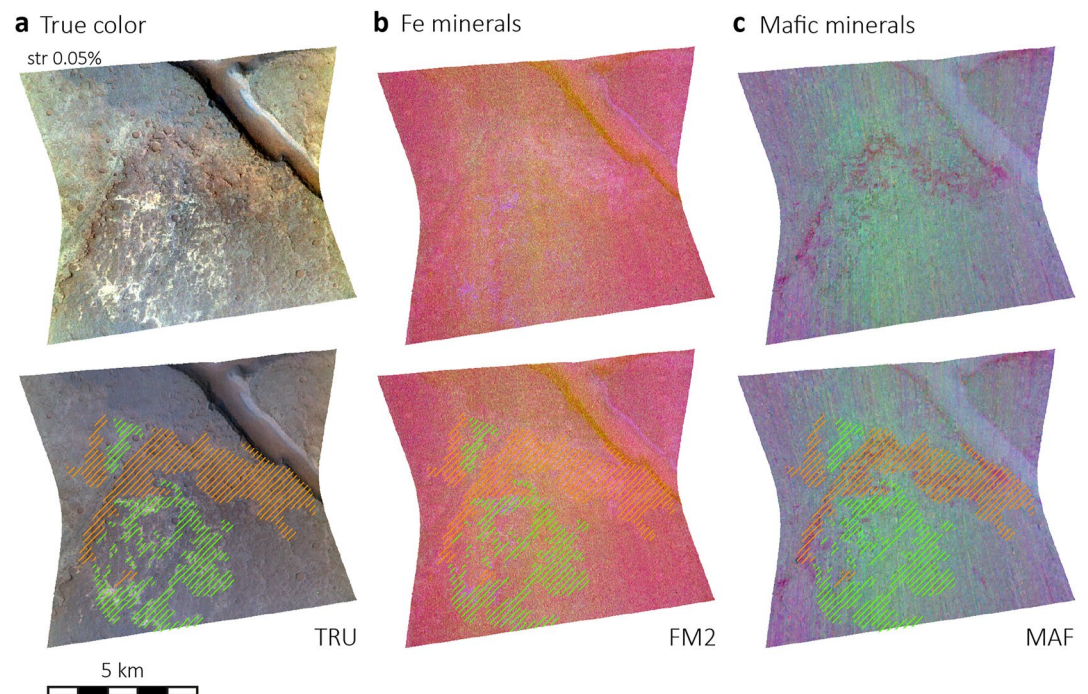
Figure 11. Composite of spectral parameters showing the area true color (TRU), the distribution of iron-rich minerals (FM2) and the distribution of mafic minerals (MAF), after Viviano-Beck et al. (2014) and Seelos (2016b). The lower panels indicate the distribution of the yellow-orange alteration zones (orange stripes) and white alteration zones (green stripes) based on CaSSIS image interpretation. (a) Red: R600 (visible, red); green: R530 (visible, green); and blue: R440 (visible, blue). The colors were slightly stretched (0.05%) in the top image to highlight color differences; the lower image gives the true colors; (b) Red: BD530_2 (0.53 μm band depth, nanophase ferric minerals); green: BD920_2 (0.92 μm band depth, crystalline ferric minerals); Blue: BDI1000VIS (1 μm integrated band depth: olivine, pyroxene, Fe-bearing glass); and (c) Red: OLINDEX3 (olivine); LCPINDEX2 (low-Ca pyroxene); HCPINDEX2 (high-Ca pyroxene).

2.59 μm band observed at Site A is observed in terrestrial clinochlore but not in a serpentine. The flared band at 2.33 μm at Site B is more reminiscent of chlorite than serpentinite. As far as spectral shapes are concerned, while the MICA serpentine type spectrum shape is particularly close to the spectrum shape of Site A at wavelengths longer than ∼2.0 μm, the chlorite type spectrum shape appears closer to the spectrum of Site B at such wavelengths (Figures 16 and 17). These figures argue in favor of CRISM detections combining serpentinite and chlorite.

Serpentine and clinochlore are green, suggesting the presence of additional minerals in the pixels where they are detected in order to explain their yellow-orange tone seen on the CaSSIS and CRISM true color images (Figures 5 and 11a, respectively). The PFM composite in Figure 12b suggests that Mg-carbonates might also be present in the yellow-orange terrain, where it would be an alternative to Fe/Mg smectites. Carbonates would potentially contribute to the yellow-orange color more significantly than Fe/Mg smectites, as illustrated by carbonates of similar yellow-orange color elsewhere on Mars (Wray et al., 2016). Furthermore, the presence of smectites in the study area is unlikely to be significant as from the CRISM spectra.

A search for carbonates was done at Sites A and B (Figure 18). Hydromagnesite, whose spectral shape in the NIR range is particularly close to that of the MICA mgs, was used as a potential analog to carbonate spectra in Nili Fossae (Ehlmann et al., 2008). At sites A and B, hydromagnesite absorptions at 2.31 and 2.51 μm (Cloutis et al., 2010) are not diagnostic and were attributed to serpentine or chlorite (Figures 16 and 17). More interesting are the absorptions observed at 3.43–3.45 and 3.86 μm, as well as the broad spectral bend centered at 3.7 μm, which echoes to the same features on the hydromagnesite library spectrum. Overall, similar to the MICA Mg-carbonate spectrum, the spectral shape of sites A and B between ∼2.1 and ∼3.9 μm follows the one of the library hydromagnesite. However, the spectral bend might alternatively correspond to an instrumental artifact (Seelos, 2016b).
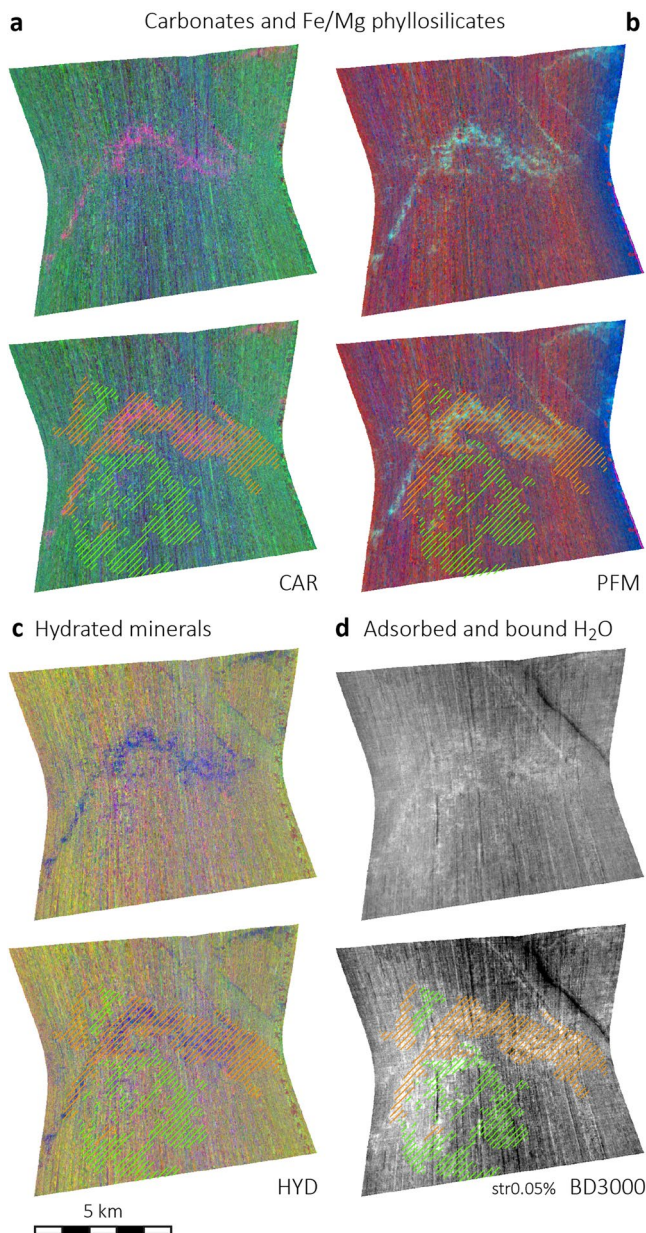
Figure 12. Composite of spectral parameters showing the carbonates versus Fe/Mg phyllosilicates (CAR and PFM) and the distribution of hydrated minerals (HYD), and the BD3000 refined spectral parameter, which shows adsorbed and bound H_2O (after Viviano-Beck et al. (2014) and Seelos (2016b)). The lower panels indicate the distribution of the yellow-orange alteration zones (orange stripes) and white alteration zones (green stripes) based on CaSSIS image interpretation. (a) Red: D2300 (2.3 μm drop-off); green: BD2500_2 (Mg carbonate); blue: BD1900_2 (1.9 μm H_2O band depth); (b) Red: BD2355 (2.35 μm band depth); green: D2300 (2.3 μm drop-off); blue: BD2290 (2.29-μm Mg, Fe-OH band depth); and (c) Parameter BD3000: Adsorbed and bound H_2O.

The CRISM measurements are consistent with the presence of Mg-carbonates such as hydromagnesite. Carbonates, in particular magnesite, were found to be 2–5 wt% of the widely distributed Martian dust (Bandfield et al., 2003), to which the East Ladon region may have contributed.

The likelihood of talc absorptions was investigated (Figure 19). There are several reasons to think that talc may be present at sites A and B. Talc has absorptions at 2.00, 2.08, and 2.31 μm, which are observed at these sites. Major absorptions at 2.39 and 2.46 μm are missing; however, they are also missing in the talc type spectrum of the MICA library (Viviano-Beck et al., 2014). The overall spectral shape at Site B is also consistent with the spectral shape of the talc from the laboratory and from the CRISM type spectrum library. The occurrence of talc at sites A and B is therefore plausible; however, it is not demonstrated, since some of the talc absorptions are shared by serpentine, chlorite, and Mg carbonate, which are more robustly identified here.

These results have two major implications. First, the yellow-orange terrain includes the same olivine and pyroxenes as the dark terrains of Units 1–3, which were subtracted by ratioing, and also serpentine, chlorite, Mg-carbonate, and perhaps talc. It appears from the similarities in the absorptions observed in Figures 16–19 (summarized in Table 4) that these minerals are mixed at the scale of CRISM pixel size, 18 m. Serpentine, chlorite, Mg carbonates, and perhaps talc are probably present in most yellow-orange ridges but in different proportions. Secondly, the serpentinite/chlorite/Mg carbonate ± talc mix is altered from a volcanic unit (Unit 1), implying that this unit is of ultramafic composition. From the spectral and geomorphological points of view, there is no criterion identified that would suggest that Units 2 and 3 are different from Unit 4, and we consider plausible that their composition is ultramafic too.

The spectral bands in the white terrain spectrum (Site C) are weak. However, the diagnostic bands of kaolinite (Bishop, Lane, et al., 2008) and its polymorphs, dickite and halloysite, may be present (Figure 20). In addition to the diagnostic bands, the white terrain displays absorption at ∼1.8 μm which is particularly well developed in dickite, commonly found along hydrothermal veins. This absorption wavelength is also found in alunite (Clark et al., 1990); however, the spectrum at Site C does not show evidence of any other absorption that would match alunite absorptions as from library spectra. Our preferred interpretation of Site C is that the aluminum phase is taken by minerals from the kaolin group, and perhaps alunite.

5. Crater Retention Age of the Lava Flows

We estimated the crater retention age of the exposed geological units using the CraterTools add-on (Kneissl et al., 2011) for ArcGIS coupled with CraterStats2 (Michael & Neukum, 2010).

In order to maximize the statistics of the age determinations, we enlarged the geologic map presented in Figure 6 (Figure 21). This allowed us to consider wider portions of the geological units to be dated.

The crater counts were carried out on three areas corresponding to Units 1, 2, and 3. The counting areas covered 553.65, 1,084.97, and 229.64 km², respectively. The age determination of Unit 2 fully meets the Warner et al. (2015) surface area requirement for reliable high resolution crater counts, whereas Units 1 and 3, although smaller than what recommended, are well above the 100 km² area considered as the reliable detection threshold by the same authors. Additionally, knowing that Unit 2, whose absolute age is the most reliable, is placed stratigraphically in
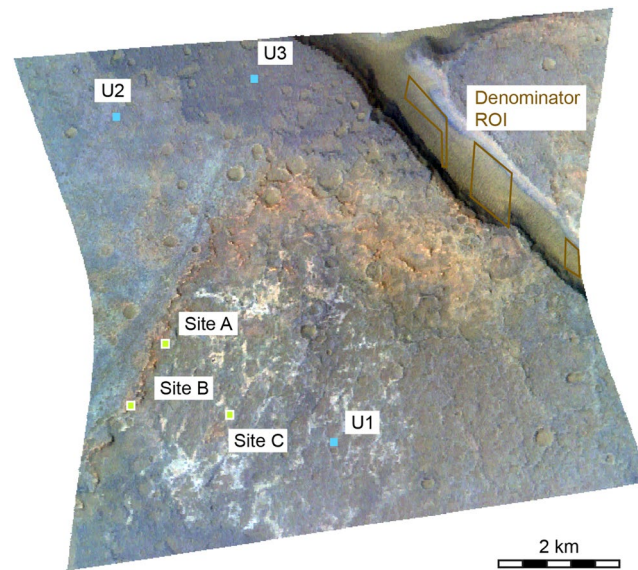
Figure 13. The location of the three pixels (representative of Unit 1, Unit 2, and Unit 3, respectively, on Figure 6) whose spectrum is displayed in Figure 14; the location of the three region of interests (ROIs) of Sites A–C (3, 7, and 44 pixels, respectively); the location of the denominator ROI (1,369 pixels) used for spectral ratioing. Coordinates are given in Section 3 in Supporting Information S1. The background Compact Reconnaissance Imaging Spectrometer for Mars image is the 67-31-11 R-G-B color composite, which approximates the colors that would be seen in a Color and Stereo Surface Imaging System NIR-PAN-BLU color composite image.

between the other two units, the absolute age of the upper and lower limits, respectively, of Units 1 and 3 is more robustly constrained.

Model ages were obtained by plotting the data using a pseudo-log binning on cumulative plots and by fitting them using the crater production function of Hartmann and Daubar (2017). The Poisson probability density function (Michael et al., 2016), in addition, was applied to elude any binning of the data and to ascertain the accuracy of the cumulative representation despite the reduced size of the counting areas. Finally, randomness analysis (Michael et al., 2011) was performed using the mean second closest neighbor distance approach to verify the spatial random distribution of the crater population.

The comparison of results obtained using (Cumulative, C) or without (Poisson, P) the binning-fitting method shows no significant divergence. The age of Unit 3 spans between 1.88 and 1.67 Ga for the C and P fitting, respectively, and ages around 2.83 (C) −2.25 (P) Ga and 3.33 (C) −3.10 (P) Ga was found for the Units 2 and 1, respectively (Figure 22).

The exposed stratigraphy of the study site starts with lava flows from the late Hesperian (Unit 1), renewed volcanic activity dated between the late Hesperian and early Amazonian (Unit 2), and again during the early Amazonian Unit 3 (Unit 3), after which erosion of the volcanic pile partly exhumed Unit 1.

6. Discussion

6.1. Outstanding Issues

The results indicate that resurfacing by lava flows of ultramafic composition of this part of the Ladon basin occurred between the late Hesperian and early Amazonian. Although spectral information is consistent with mafic volcanism as well, alteration to serpentine favors emplacement of ultramafic flows. Alteration of the source rock occurred through a dike and vein system (e.g., Gudmundsson et al., 2002). These results raise several issues.

- First, serpentinization occurs in oceanic crust on Earth and is visible today in ophiolites. Ophiolites are unlikely on Mars, and another mechanism for serpentinization is needed.
- Second, the serpentine, chlorite, carbonate, and talc signatures are observed at topographic highs within an eroded lava flow, usually in the form of yellow-orange linear *ridges* (Figures 7–9). However, the walls of
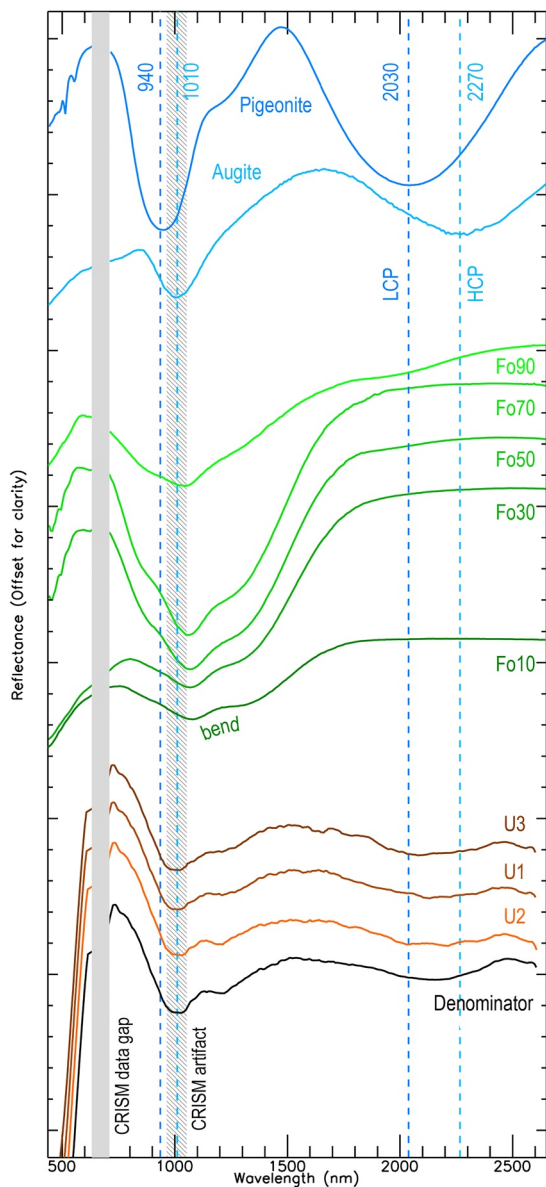
Figure 14. Comparison between spectral characteristic representative of the three dark terrain units (U1-3, located in Figure 13; coordinates are in Section 3 in Supporting Information S1), and spectral characteristics of some end-member pyroxenes (low to high-Ca) and olivines (ferrous to Mg-rich). The Compact Reconnaissance Imaging Spectrometer for Mars spectra were mobile-averaged with an 11-channel box to smooth noise while enhancing large-scale variations. The library spectrum of augite (NMNH120049) is from the USGS spectral library (Kokaly et al., 2017), and the other library spectra (pigeonite DL-CMP-008-A, olivine spectra) are from RELAB (R. E. Milliken et al., 2016). The olivine spectra (Fo10, Fo30, Fo50, Fo70, and Fo90) were studied by Dyar et al. (2009).

the graben in the studied area distinctly show that the yellow-orange level is an alteration *layer*. This layer is thus to include resistant ridges in a weaker matrix. A strengthening mechanism is required.

- The pixel size of the CRISM cube is 18 m. The detected serpentine, chlorite, carbonates, and talc are representative of yellow-orange terrain exposed as ridges usually not thicker than meters. Some minerals are more apparent at Site A and others at Site B. This implies that these minerals are closely distributed in the field. They are mixed in the CRISM pixels, with some of them more emphasized at some sites (e.g., A) and others more emphasized at other sites (e.g., B).

- Ridge orientation emphasizes that their formation was influenced by the ambient stress field. They are observed to be fully brecciated, and their mineralogy suggests a magmatic origin. Nevertheless, interpreting them as dikes or veins is not without issues. A satisfactory mechanism of formation needs to be found.

- Kaolin polymorphs, found in the white terrain, may form in listwanite systems, but may also have a distinct origin. HiRISE image observation shows that the white terrain occurs within topographic lows.

6.2. Listwanitization

We suggest that the yellow-orange terrain is formed using hydrothermal processes akin to listwanitization. The term *listwanite* has been used to describe a variety of rock types; here we follow the broad definition suggested by Ash (2001), according to which listwanite is a descriptive term that characterizes the full range of genetically related assemblage of minerals formed by hydrothermal alteration of ultramafic rocks. Listwanite therefore includes a range of rocks such as serpentinites as well as silica-carbonate derived products such as carbonate rocks, talc, and quartz. Of these minerals, only quartz was not found, which may be explained by the flat reflectance of quartz in the CRISM spectral range. Ophiolite is the prominent natural geologic context of listwanites on the continental Earth. Serpentinization is an oceanic process; in contrast, carbonation commonly occurs on land after ophiolite obduction by subaerial weathering, as shown by depth-dependent listwanitization in the Semail ophiolite and the absence of deformation listwanite fabric in the Bir Umq ophiolite (Gahlan et al., 2022; Kelemen et al., 2011). However, submarine carbonation at some oceanic ridges makes atmospheric contribution not mandatory. Listwanite is also intimately related to tectonic deformation; it has been described in thrust systems (Ash & Arksley, 1990; Hansen et al., 2005; L. Zhang et al., 2015; Sherlock & Logan, 1995; Xiangzhen et al., 2009); as well as along large shear zones (Qiu & Zhu, 2015; Robinson et al., 2005).

Listwanitization in Ladon would provide a framework for the coexistence of resistant yellow-orange ridges and a hosting weaker layer, such as illustrated in Figures 7d and 7f, and also their color, which would be chiefly due to carbonates (Wray et al., 2016). Listwanite ridges are commonly observed within serpentinite massifs; their topography is a consequence of silicification. The silica-carbonate assemblages of listwanite are fracture-controlled ("dike-like bodies," Hamdy et al., 2022) and depend on temperature gradients, with serpentine and carbonates developing at higher temperature and silica (usually quartz) at lower temperature along fractured pathways (Ash, 2001; Azer, 2013; Falk & Kelemen, 2015; L. Zhang et al., 2015; Robinson et al., 2005; Sherlock & Logan, 1995) following mechanisms detailed by Stanger (1985), Buckman and Ashley (2010), and Ulrich et al. (2014).
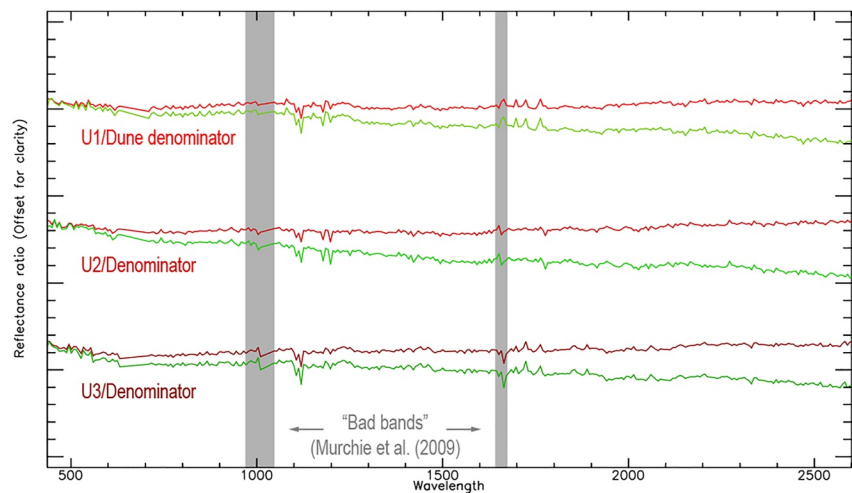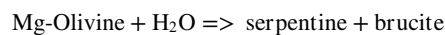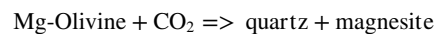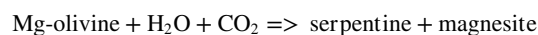
Figure 15. Ratioed spectra of dark terrain (U1, U2, and U3 for Unit 1, Unit 2, and Unit 3, respectively). The ratioed spectra are almost flat (green lines) and become flat after continuum removal (red lines). Contrary to Figure 14, the spectra were not mobile-averaged.
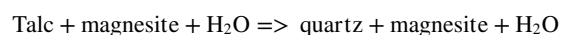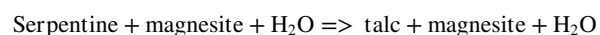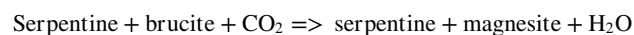
Yellow-orange listwanite ridges looking similar to those in East Ladon are strengthened by silica and were described for instance at the Sartohay ophiolite along the Dalabute shear zone in Xinjiang (Buckman & Ashley, 2010; Qiu & Zhu, 2015; Robinson et al., 2005), the Luobusa ophiolite along the Tsangpo suture (L. Zhang et al., 2015; Xiangzhen et al., 2009), the Semail ophiolite in Oman (Falk & Kelemen, 2015), the ophiolites of Eastern (Hamdy et al., 2022) and South Eastern (Azer, 2013) Deserts of Egypt, and at the Bir Umq ophiolite in Arabia (Gahlan et al., 2022). Listwanite ridges are usually meters to tens of meters high, similar to those observed in Ladon but may be as high as a few hundred meters, as seen in the Semail ophiolites.

The serpentinization of ultramafic rocks and silica-carbonation of listwanites involve a broad range of chemical reactions, with olivine, pyroxene, and plagioclase as the sources, as well as reservoirs of H_2O and CO_2, which may or may not include the atmosphere. Serpentine is a secondary source from which carbonates and quartz are derived, as well as other mineral species, such as talc. Kelemen et al. (2011) synthesize many of them. Chlorite may result from the solid-state transformation of serpentinite (H. Zhang et al., 2021).

Some of the chemical reactions (Kelemen et al., 2011) that may be relevant to the studied Ladon area are as follows:

$$\text{Mg-olivine} + H_2O + CO_2 \Rightarrow \text{serpentine} + \text{magnesite}$$

$$\text{Mg-olivine} + H_2O + CO_2 \Rightarrow \text{talc} + \text{magnesite}$$

$$\text{Mg-Olivine} + CO_2 \Rightarrow \text{quartz} + \text{magnesite}$$

$$\text{Mg-Olivine} + H_2O \Rightarrow \text{serpentine} + \text{brucite}$$

Brucite is metastable and may react further as follows:

$$\text{Serpentine} + \text{brucite} + CO_2 \Rightarrow \text{serpentine} + \text{magnesite} + H_2O$$

$$\text{Serpentine} + \text{magnesite} + H_2O \Rightarrow \text{talc} + \text{magnesite} + H_2O$$

$$\text{Talc} + \text{magnesite} + H_2O \Rightarrow \text{quartz} + \text{magnesite} + H_2O$$

Some chemical reactions involve pyroxene, for instance:

$$\text{Mg-olivine} + \text{High-Ca pyroxene} + H_2O + CO_2 \Rightarrow \text{serpentine} + \text{calcite}$$

$$\text{Mg-olivine} + \text{High-Ca pyroxene} + H_2O \Rightarrow \text{serpentine} + \text{Ca(aq)} + OH, \text{then}$$

Figure 16.

$$Ca(aq) + OH + CO_2 => CaCO_3 + H_2O$$
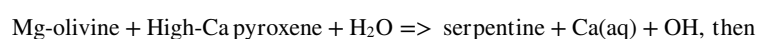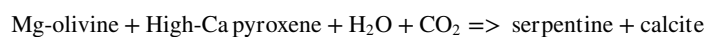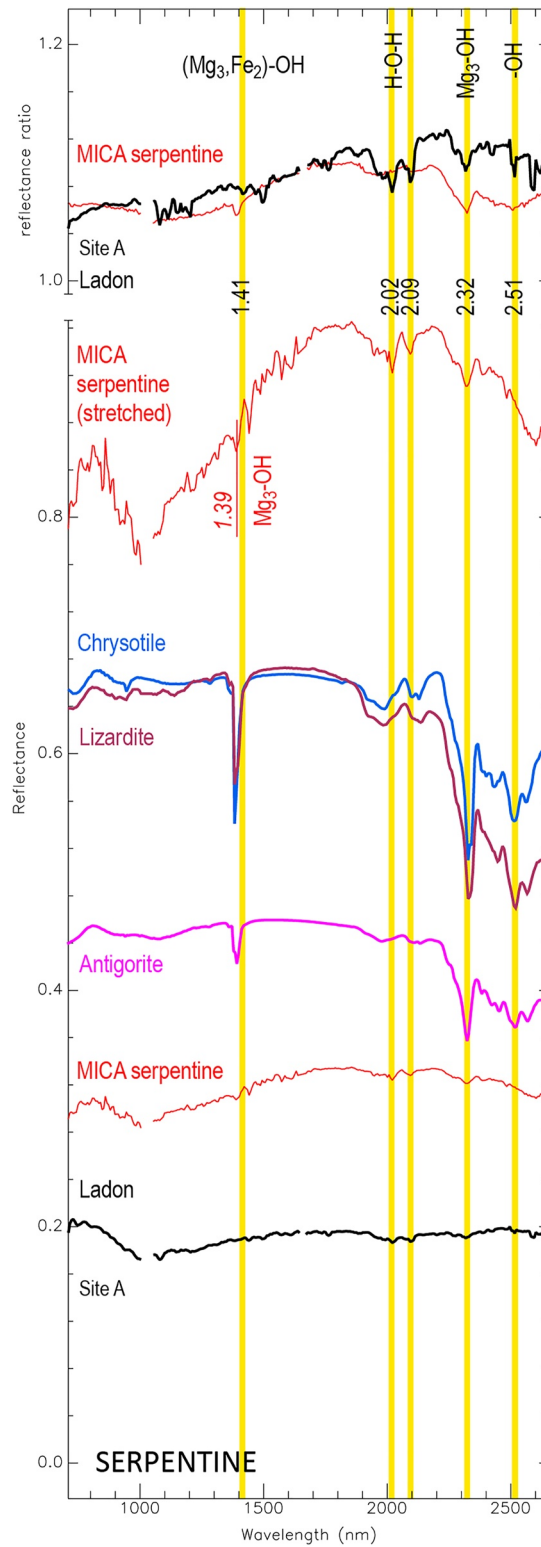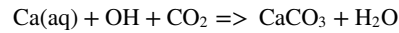
The following reaction was proposed by Sherlock and Logan (1995):

$$Serpentine + H_2CO_3\ (aq) + H_4SiO_4\ (aq) => magnesite + water + quartz$$

In these reactions, Fe may add or substitute to Mg in olivine, for instance (Templeton & Ellison, 2020):

$$Ferroan\ brucite + SiO_2\ (aq) + H_2O => Fe\text{-}serpentine + H_2$$
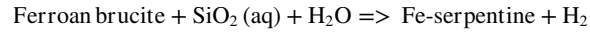
Iron may also be incorporated in hydroxides, for instance (Kelemen et al., 2011; Templeton & Ellison, 2020):

$$Fe\text{-}olivine + H_2O => Fe\text{-}serpentine + magnetite + H_2(aq)$$

$$Ferroan\ brucite => magnetite + H_2 + H_2O$$
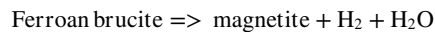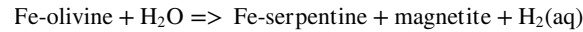
Hansen et al. (2005) summarized the most significant succession of reactions involved in listwanitization:

$$Serpentine + /\!- olivine + /\!- brucite => serpentine + magnesite => talc + magnesite => quartz + magnesite$$

These reactions illustrate the diversity of processes potentially at work during listwanitization. Serpentine, chlorite, Mg carbonate, and talc are the major compounds of the reactions, in agreement with the spectral analysis results presented in Figures 16–19. They also show that the strength of the yellow-orange ridge in the Ladon basin via listwanitization could be explained if quartz is present at Sites A-B.

6.3. Occurrence of Quartz

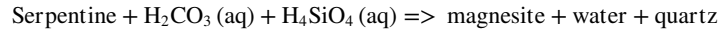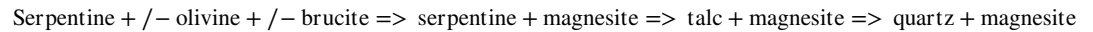Quartz is an end product of alteration of olivine, pyroxene, plagioclase, and serpentine. Due to its flat spectral shape in the CRISM range, its detectability relies on its high reflectance compared to many other minerals in this range. Its presence cannot be demonstrated; nevertheless, it could be present in the white bright terrains in greater proportion but anywhere else in the altered rocks.

6.4. Consistency Between the Spectral Absorptions, Spectral Parameters, and *K*-Mean Analysis

Comparison between the CRISM spectral parameters and the K-mean analysis of the CaSSIS image shows that although the whole surface area covered by the CRISM cube is covered by ferric oxides at the CaSSIS scale, this widespread distribution goes with variations that depend on topography.

The interpretations based on the spectral absorptions make it possible to interpret the spectral parameters further. Spectral absorption analysis shows that olivine and pyroxenes are found throughout the cube, whereas the spectral parameters indicate that pyroxenes are absent in the yellow-orange area (Figure 11c). This apparent conflict is explained by our approach, in which the broad spectral variations of olivine and pyroxene are included in the spectral ratio denominator. This made it possible to separate their spectral contribution from the contribution of the narrow absorptions of alteration minerals in the same spectral range. The broad absorption of olivine occurs around 1 μm (Figure 14), far from the major absorption bands of alteration minerals, which start at ~1.4 μm and mainly occur after 1.9 μm. Olivine is therefore not masked by the alteration mineral absorptions. In the contrary, the broad absorption of pyroxenes occurs in the range 1.5–2.8 μm, covering most of the area where alteration minerals sign in the CRISM range. LCPINDEX2 and HCPINDEX2 are exclusively based on the band centers, making these minerals detectable.

Figure 16. Comparison between the spectra of the yellow-orange terrain at Site A and the laboratory spectra of serpentinite. Details on the library spectra are found in Bishop et al. (2002) (lizardite C53/JB526), Bishop, Dyar, et al. (2008) (antigorite JB559), and Bishop, Lane, et al. (2008) (chrysotile JB732). The lower part of the plot shows absolute reflectance spectra, and the upper part shows ratioed reflectance spectra using the dune field region of interest as the denominator. The type serpentine I/F spectrum selected in the Minerals Identified through CRISM Analysis (MICA) library (Viviano-Beck et al., 2014) is in red. The unratioed serpentine I/F spectrum in the middle of the plot is the same as the one at the bottom of the plot except that the amplitude of reflectance was stretched four times and the spectrum was offset for easier comparison with the ratioed Ladon spectra. The Compact Reconnaissance Imaging Spectrometer for Mars IR data in the range 1,002–1,047 nm and around 1,650 nm may contain erroneous information (S. L. Murchie et al., 2009) and were removed. The mobile average box size for the Ladon spectrum is three channels.

Figure 17.

The PFM composite image showing the yellow-orange areas in blue (Figure 12c) may be interpreted either as Fe/Mg smectite or Mg carbonate. Spectral analysis could not reveal smectite absorption features; however, Figure 18 shows that Mg carbonates are likely present. We therefore interpret the blue color of the yellow-orange areas on the PFM image as a plausible contribution of Mg-carbonates rather than smectites (Table 3).

Figure 18. Comparison between the spectra of the yellow-orange terrain at Sites A and B and library spectra of hydromagnesite (CRB208, RELAB spectral library, R. E. Milliken et al., 2016). The type Mg-carbonate I/F spectrum selected in the Minerals Identified through CRISM Analysis (MICA) library (Viviano-Beck et al., 2014) is in red. The yellow lines correspond to hydromagnesite absorptions. The wavelengths of the deepest absorptions at Sites A and B are indicated but do not significantly emerge from the spectral noise and might be noise as well. The Compact Reconnaissance Imaging Spectrometer for Mars IR data in the ranges 1,002–1,047 nm, 2,800 nm, and around 1,650 and 2,800 nm may contain erroneous information (S. L. Murchie et al., 2009) and were removed.

The water detected by the BD3000 spectral parameter (Figure 12d) may be explained in the yellow-orange areas by the incorporation of water into the Mg carbonate structure, leading to hydromagnesite (Table 3) of formula $Mg_5(CO_3)_4(OH)_2 \cdot 4 H_2O$. The BD3000 parameters indicate that the white terrain also contains hydrated minerals. This seems to conflict with our preferred interpretation for the composition of the white terrain at Site C, which from the spectral absorptions would expose minerals from the kaolin group. However, the absorption at 1.8 µm (Figure 20) at Site C may reconcile the spectral parameters with the spectral absorption analysis, if it testifies to the exposure of alunite, $KAl_3(SO_4)_2(OH)_6$ in addition to the kaolin group minerals. These interpretations are fragile and ascertaining the composition of the white alteration level will need an examination of similar terrain in other CRISM cubes.

6.5. Comparison Between the Linear Ridges and Some Terrestrial Listwanite Ridges

In order to evaluate further the plausibility that the yellow ridges are listwanite, we compared the spectra of sites A and B with the spectra of some terrestrial listwanite ridges measured by the Terra/Advanced Airborne Thermal Emission and Reflection Radiometer (ASTER) multispectral instrument. Five ASTER channels frame the wavelength of the strongest carbonate absorption, at ∼2.3 µm, that can be found in the near-infrared range <2.5 µm. These channels are located at 2.165 ± 0.02, 2.205 ± 0.02, 2.260 ± 0.025, 2.330 ± 0.035, and 2.395 ± 0.035 µm. ASTER surface reflectance of two ophiolite sites where listwanitization occurred are shown in Figure 23. Four other sites are shown in Section 4 in Supporting Information S1.

Listwanite at the six ophiolite sites is characterized by a blue spectral slope between 1.656 and 2.167 µm, and clear absorption at 3.33 µm (Figure 24). After continuum removal, the CRISM spectra of the sites A and B appear close to the ASTER spectra, confirming the plausibility that the ridges have a listwanitic composition.

6.6. Significance of the White Terrain

Olivine and pyroxene were detected in the CRISM data; however, it is likely that plagioclase is also present. It was shown that the abundance of olivine and pyroxene relative to plagioclase in mafic or ultramafic rock hampers plagioclase detection (see a discussion in Viviano-Beck et al., 2017). Listwanitization may include crystallization of kaolinite (e.g., Gahlan et al., 2022) but it has not been frequently reported. There is also no geomorphological evidence from the HiRISE and CaSSIS images that the white and yellow-orange terrains share a common genesis. We suggest that plagioclase dissolution (Casey et al., 1991) by acidic water was involved in the formation of the detected kaolinite via the reaction (after Wawersik et al. (2001) and Hangx and Spiers (2009)):

Figure 17. Comparison between the spectra of the yellow-orange terrain at Site A and the library spectra of chlorite. Details on the library spectra are found in Bishop, Lane, et al. (2008) (chamosite JB739, Clinochlore JB738). The lower part of the plot shows absolute reflectance spectra and the upper part shows ratioed reflectance spectra using the dune field region of interest as the denominator. The type chlorite I/F spectrum selected in the Minerals Identified through CRISM Analysis (MICA) library (Viviano-Beck et al., 2014) is in red. The unratioed chlorite I/F spectrum in the middle of the plot is the same as that at the bottom of the plot except that the amplitude of reflectance was stretched four times and the spectrum was offset for easier comparison with the ratioed Ladon spectra. "sh" stands for "shoulder." The Compact Reconnaissance Imaging Spectrometer for Mars IR data in the range 1,002–1,047 nm and around 1,650 nm may contain erroneous information (S. L. Murchie et al., 2009) and were removed. The mobile average box size for the Ladon spectrum is three channels.
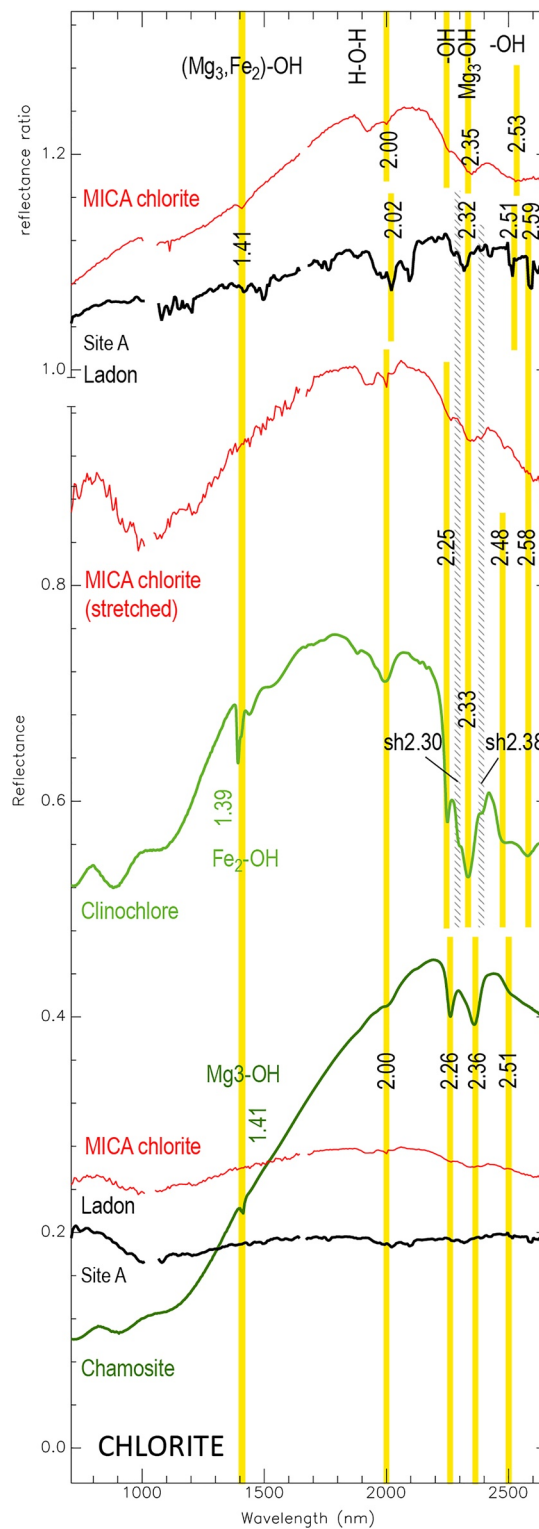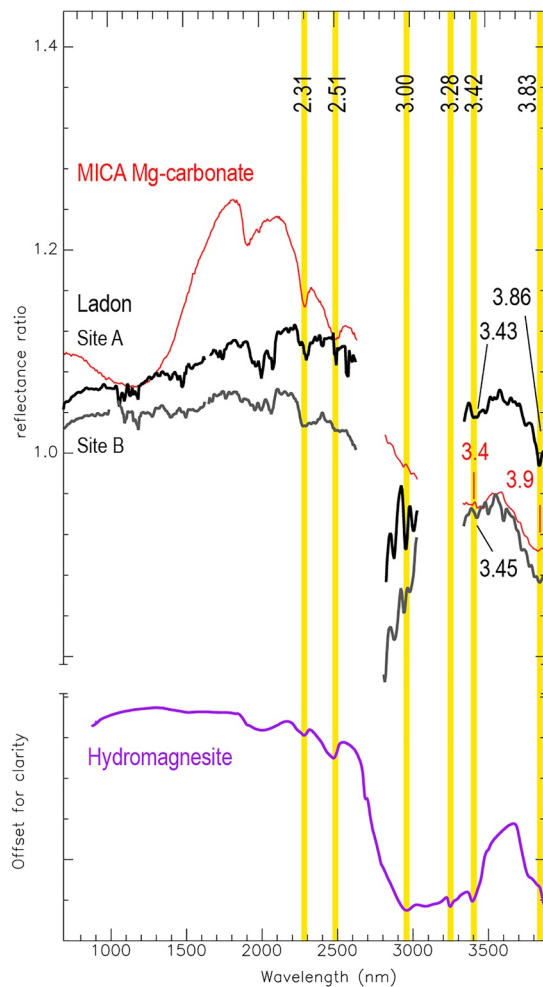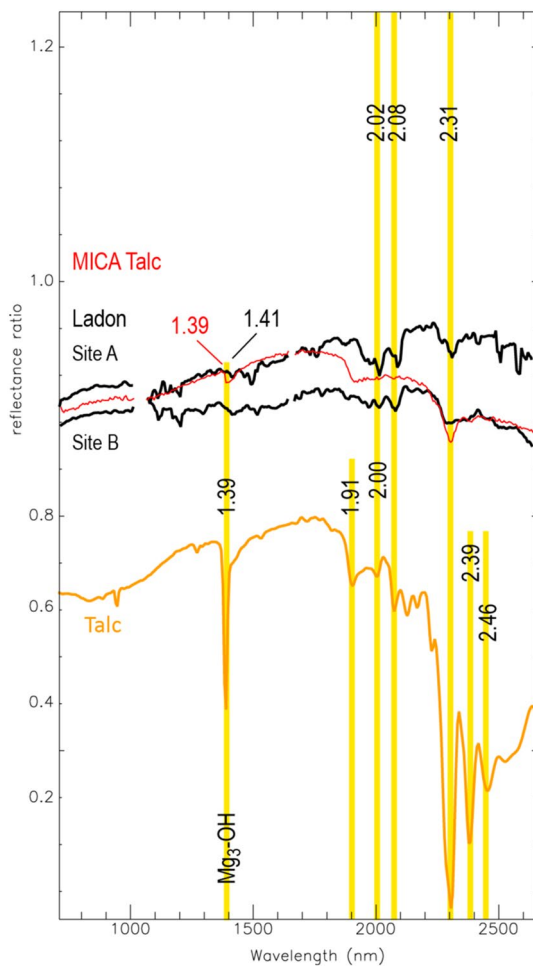
Figure 19. Comparison between the spectra of the yellow-orange terrain (Sites A and B) and library spectra of talc (GDS23, splib07a spectral library, Kokaly et al., 2017). In red is the type talc I/F spectrum selected in the Minerals Identified through CRISM Analysis (MICA) library (Viviano-Beck et al., 2014). The yellow lines correspond to the talc absorptions. The Compact Reconnaissance Imaging Spectrometer for Mars IR data in the ranges 1,002–1,047 nm, 2,800 and around 1,650 and 2,800 nm may contain erroneous information (S. L. Murchie et al., 2009) and were removed.

$$\text{Anorthite} + \text{water} => \text{Ca}^{2+} + \text{kaolin polymorph}$$
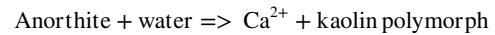
Although kaolinite is the only stable kaolin phase (De Ligny & Navrotsky, 1999), by order of increasing temperature, the forming polymorph would be halloysite (<100°C), then kaolinite, and dickite until ~300°C (Bauluz, 2015; Zotov et al., 1998). Dickite would be the most adapted to the hydrothermal conditions of listwanitization and yellow-orange terrain formation. Slow conversion of halloysite and dickite to kaolinite might result in kaolinite being the main polymorph observed today.

Ece et al. (2013) proposed a mechanism for the development of a kaolinite-alunite facies from the dissolution of feldspar and volcanic glass in low to intermediate hydrothermal conditions at low pH. This model may be a starting point to investigate the possible coexistence of kaolin group minerals and alunite at Site C, as well as other areas on Mars where similar white terrain is identified.

6.7. Listwanitization in the Regional Framework

The age of Units 1 and 2, from late Hesperian to early Amazonian, is younger than expected from broader scale mapping by Irwin and Grant (2013), in which these units (HNb2 and Hb3) are ascribed an upper Noachian to early Hesperian age. Weitz et al. (2022) reported on fluvial erosion and deposition of light-toned layered deposits of similar age in many sites of the Ladon basin west of our study area. These layered deposits, which include smectites and other hydrated minerals, were not observed in our study area. However, fluvial activity may have provided the source or part of the source of water required for serpentinization, carbonation, and kaolinization. An older groundwater reservoir might also have been tapped (Grant & Parker, 2002).

The results presented here corroborate other studies that advocate a late magmatic insurgence in the Ladon basin. Following the experimental results obtained by Luzzi et al. (2021), the general radial and concentric distribution of grabens centered at the western part of the basin, as well as their T and Y-shaped junctions, would testify to such a late magmatic activity causing oblate extension and diffused fissure eruptions. Similarly, the abundance of FFCs in the close vicinity of the East Ladon study area (Figure 2) would testify to the nearby emplacement of magmatic bodies, whether sills or laccoliths, which could share a common magmatic source with Units 1–3 in this work.

As a hydrothermal process usually involving a huge volume of rock, listwanitization was found on Earth to influence the crustal magnetic record. In many environments, hydrothermal activity tends to suppress magnetization (Choe et al., 2021; Szitkar, Dyment, Choi, & Fouquet, 2014). In ultramafic rocks, in contrast, the titanomagnetite formed during the serpentinization process tends to strengthen crustal magnetization (Szitkar, Dyment, Fouquet, et al., 2014). Listwanitization then attenuates the magnetization (Tominaga et al., 2017). Quesnel et al. (2009) insist on the role of serpentinization as a pre-Noachian source of Martian crustal magnetization. The eastern Ladon basin, located in a region of the highlands where strong magnetic anomalies are observed, is a magnetic low compared to its surrounding toward West, North, and East (Langlais et al., 2019). Late magmatic activity below the FFC, in the absence of a magnetic field, and listwanitization in East Ladon might be causes of partial crustal demagnetization in this area.

Listwanite is a major source for some metals on Earth, in particular native Au and Cr but also, depending on the geological context, other rare (As, Hg, and Ni) and base (Cu, Pb, Sb, and Zn) metals as well as sulphides (Ash & Arksley, 1990; Azer, 2013; Ferenc et al., 2016; L. Zhang et al., 2015; Qiu & Zhu, 2015; Sherlock & Logan, 1995; Xiangzhen et al., 2009). The occurrence of these deposits is closely related to the geochemical reservoir tapped by

Table 4
Summary of the Spectral Absorptions Used in This Work for Mineral Identification

Mineral	Site	Absorption band centers (μm)											Spectral shape similarity	
													In the range 1–2.6 μm[a]	In the range 2.1–3.9 μm[a]
Serpentine	A	1.41			2.02	2.09	2.32		2.51				Reasonably similar	
	B	1.41			2.02	2.09	2.32		2.51				Reasonably similar until 2.3 μm	
Chlorite	A	1.41			2.02		2.32		2.51	2.58/2.59			Reasonably similar until 2.3 μm	
	B	1.41			2.02	2.09	2.32		2.51	2.58/2.59			Reasonably similar	
Mg-carbonate	A						2.31		2.51		3.42/3.43	3.83/3.86		Reasonably similar
	B						2.31		2.51		3.42/3.45	3.83/3.86		
Talc	A				2.00/2.02	2.08/2.09	2.31						Reasonably similar until 2.3 μm	
	B				2.00/2.02	2.08/2.09	2.31						Reasonably similar until 2.3 μm	
Kaolin minerals	C	1.39–1.41		1.92	2.17–2.21			2.45	2.50				Reasonably similar after 1.7 μm	
Alunite?	C		1.80											

Note. Band center differences between library spectra and Compact Reconnaissance Imaging Spectrometer for Mars detections are indicated as a fraction, with library spectrum center as the numerator and the detected center as the denominator. The library spectra are those shown in Figures 16–20.
[a]Outside of the degraded spectral channels as identified by Murchie et al. (2009) and Seelos (2016a, 2016b).

the ultramafic magmas, but this diversity and their economic interest suggest that East Ladon might be a priority target to check in a search for mineral resources on Mars.

6.8. Proposed Geologic Model

The geological section of Figure 25 is an interpretative synthesis of our findings. In the first order, olivine and pyroxene characterize all the mapped geological units. This is reflected in all the rocks having low albedo. Unit 1 includes the yellow-orange terrain in which serpentinite, chlorite, and perhaps carbonate and talc are found, as well as the kaolin minerals and perhaps alunite in the white terrain. The red structures account for the silicified listwanite ridges.

The age of alteration is constrained by the following observations:

- The yellow and white layers observed on the graben walls are restricted to Unit 1, they formed, therefore, after Unit 1.
- Because the yellow terrain is interpreted to be of hydrothermal origin, it needs to be connected to a crustal warming source. The warming source is interpreted to be Unit 3 rather than in the deeper crust for two reasons. First, the graben walls do not show any layer perturbation at a depth below the yellow and white layers nor any
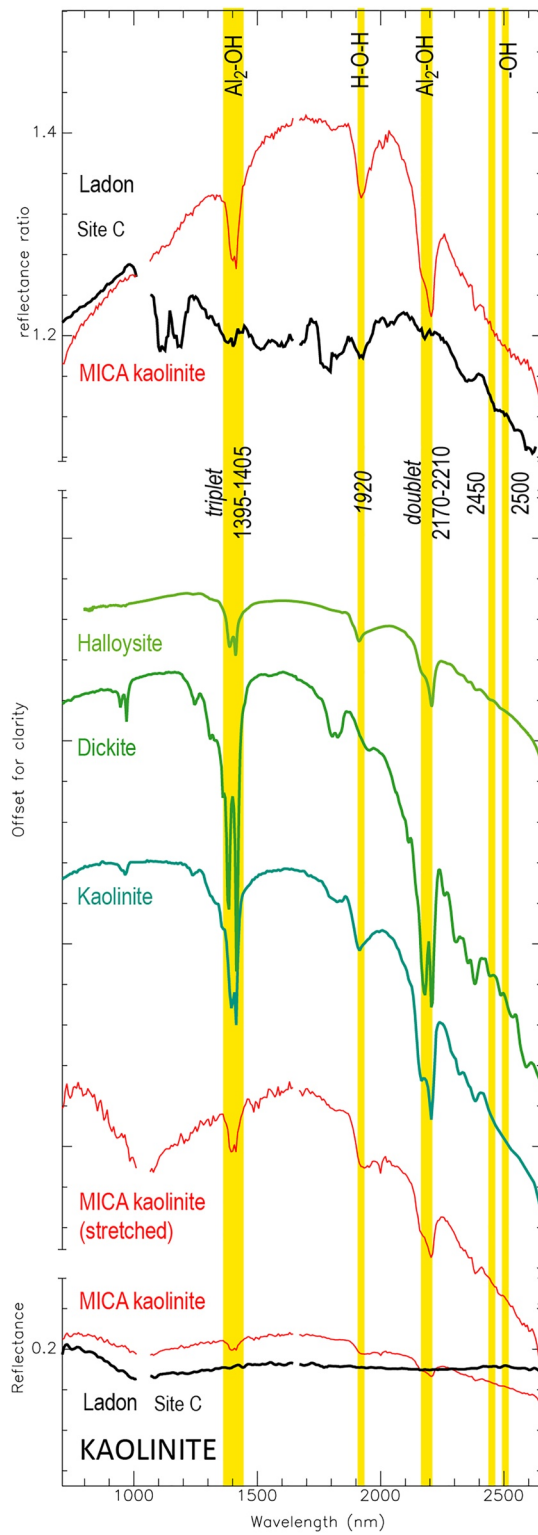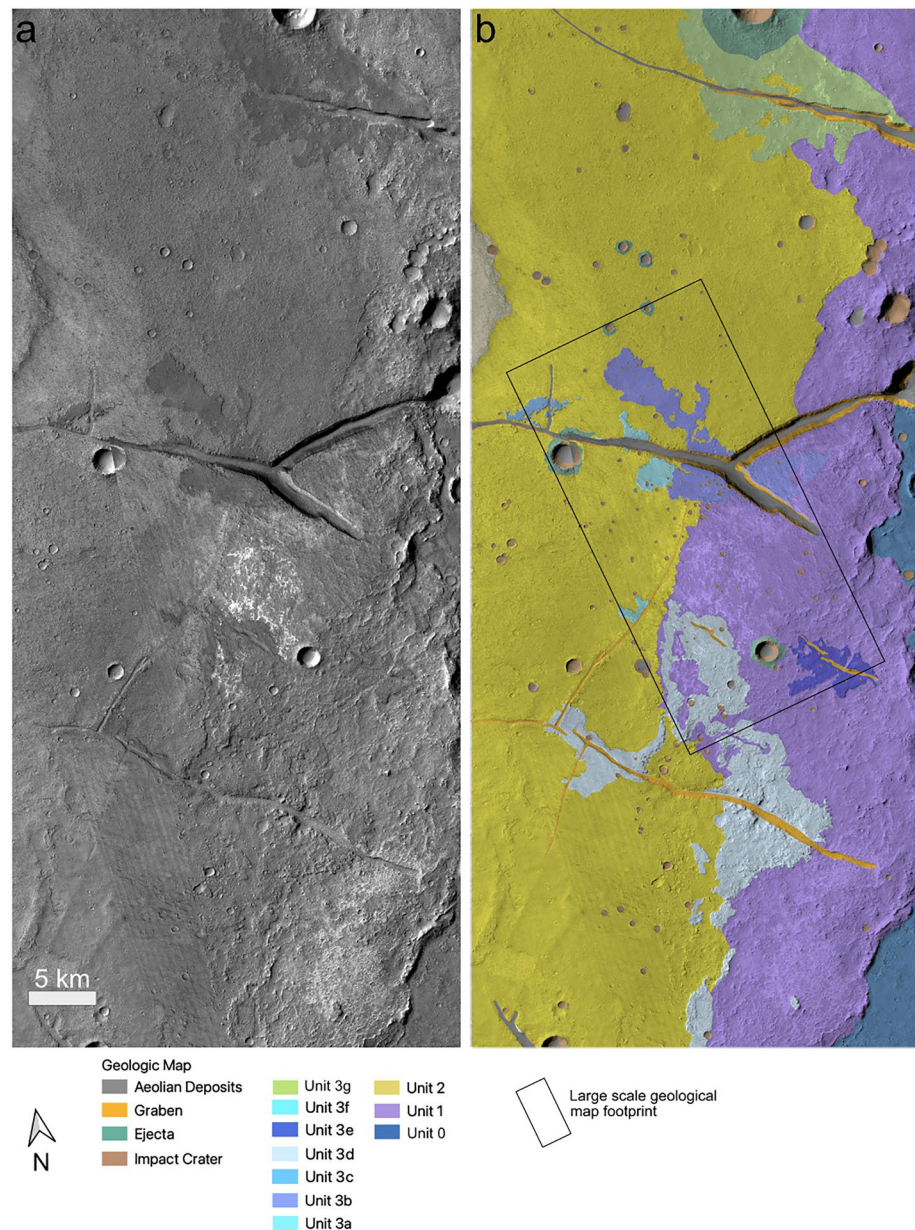
Figure 20.

Figure 21. (a) Context Global mosaic version beta01 from Murray Lab (Dickson et al., 2018) used for the enlargement of the geologic mapping of the East Ladon study site; (b) enlarged geological map. The black box in panel (b) delimits the geological map shown in Figure 6. Unit numbers increase inversely to their relative age; letters indicate distinct outcrops for the same unit.

Figure 20. Comparison between the spectra of the white terrain (Site C) and library spectra of kaolinite (CM3, USGS spectral library, Kokaly et al., 2007), dickite (H-14, RELAB spectral library, R. E. Milliken et al., 2016), and halloysite (JB-JLB-A47, RELAB spectral library, R. E. Milliken et al., 2016). The lower part of the plot shows absolute reflectance spectra and the upper part shows ratioed reflectance spectra using the dune field region of interest as the denominator. The type kaolinite I/F spectrum selected in the Minerals Identified through CRISM Analysis (MICA) library (Viviano-Beck et al., 2014) is in red. The middle kaolinite I/F spectrum is the same as the one at the bottom spectrum except that the amplitude of reflectance was stretched four times and the spectrum was offset for easier comparison with the ratioed Ladon spectra. The absorption bands centered at 2,450 and 2,500 nm are apparent at Site C after continuum removal. The Compact Reconnaissance Imaging Spectrometer for Mars IR data in the range 1,002–1,047 nm and around 1,650 nm may contain erroneous information (S. L. Murchie et al., 2009) and were removed. The mobile average box size for the Ladon spectrum is seven channels.
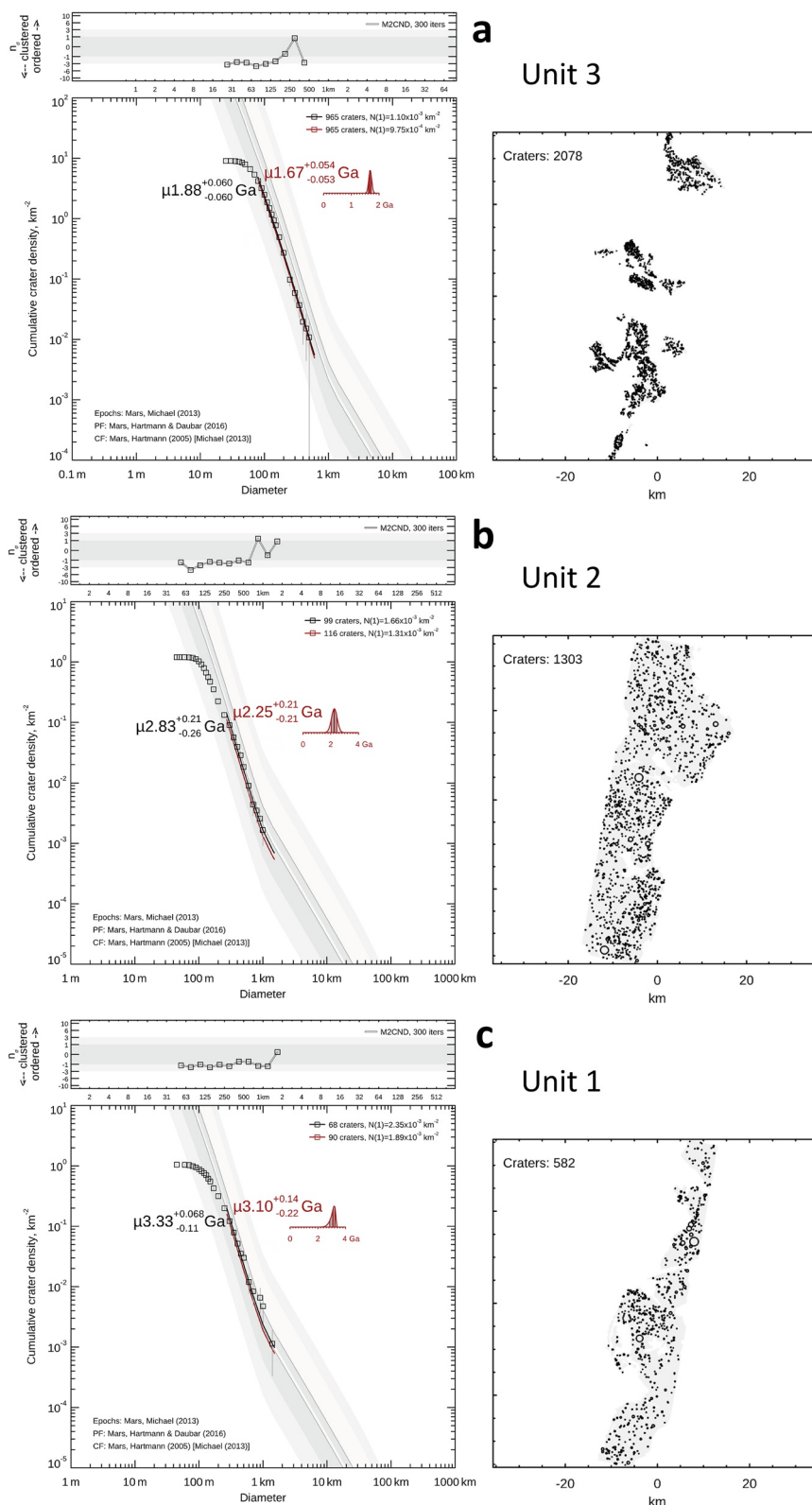
Figure 22. Model age determinations and counting areas for (a) Unit 3, (b) Unit 2, and (c) Unit 1 from the geologic map in Figure 21. The black and red fits represent the cumulative production function and the Poisson probability density function, respectively. Panels above the age plots show the randomness analysis results.
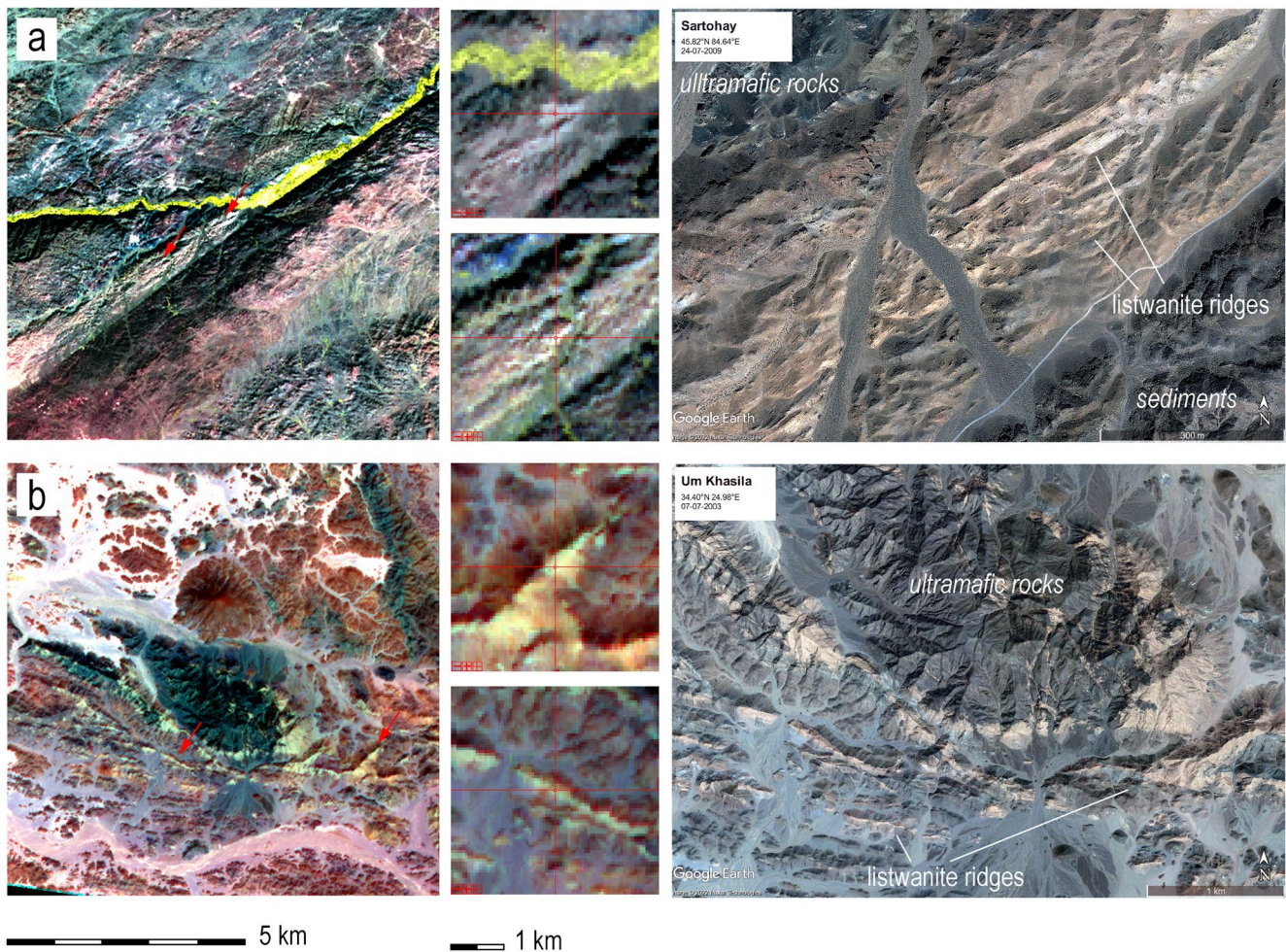
Figure 23. ASTER multispectral scenes and Maxar images of listwanite ridges on Earth, located at (a) Sartohay, Xinjiang Proince, China, and (b) Um Khasila, Eastern Desert of Egypt. Left: ASTER scene, color composite of bands 8-3N-1 (2.330 ± 0.07 µm, 30 m/pixel; 0.820 ± 0.04, 15 m/pixel; 0.560 ± 0.04 µm; 15 m/pixel). The arrows point to the areas where spectral measurements were done. Middle: Location of the spectral measurements shown in Figure 24. Right: High-resolution views of the listwanite ridges, from Google and ©2022 Maxar Technologies.

clue that would suggest interactions with a warming source depth. Unit 2 is very thin; as a consequence, the warming source is likely to be Unit 3. Second, mapping has revealed that hydrothermal alteration frequently followed portions of the rims of the largest craters in the study area, suggesting that some of the fluids passively followed the existing structures. As a corollary, the driving pressure during the propagation of the hydrothermal fluids was low, though still high enough to reopen fractures not favorably oriented with respect to the orientation of the principal stresses. This is consistent with fluid flow in response to a nearby, local event, such as the emplacement of the overlying Unit 3, but less likely in the case of a deep, regional event, such as magma chamber intrusion.

- Such a connection between Unit 3 and hydrothermal alteration underneath implies that Unit 3 once covered the whole area above the yellow and white units. The lobate fronts of Unit 3 are more likely erosional than pristine. This hypothesis is supported first by the yellow ridges themselves. There are few geologic processes that generate similar linear ridges up to tens of meters high in the open air. The most frequent are subglacial ridges, which are here not relevant due to the absence of observation of a glacial land system. Second, the geomorphology of Unit 1 is erosional, exemplified by the geomorphology of many rimless impact craters. Third, the effusion temperature of ultramafic flows is in the range 1600–1800°C. At the contact area with the ground, ultramafic magma temperature may be as high as 1200°C, which is so efficient in warming the subsurface that the ground can be thermally eroded by meters to hundreds of meters (Huppert & Sparks, 1985). We conclude that the emplacement of Unit 3 is a plausible trigger of hydrothermal activity, should groundwater be present at depths of tens of meters.
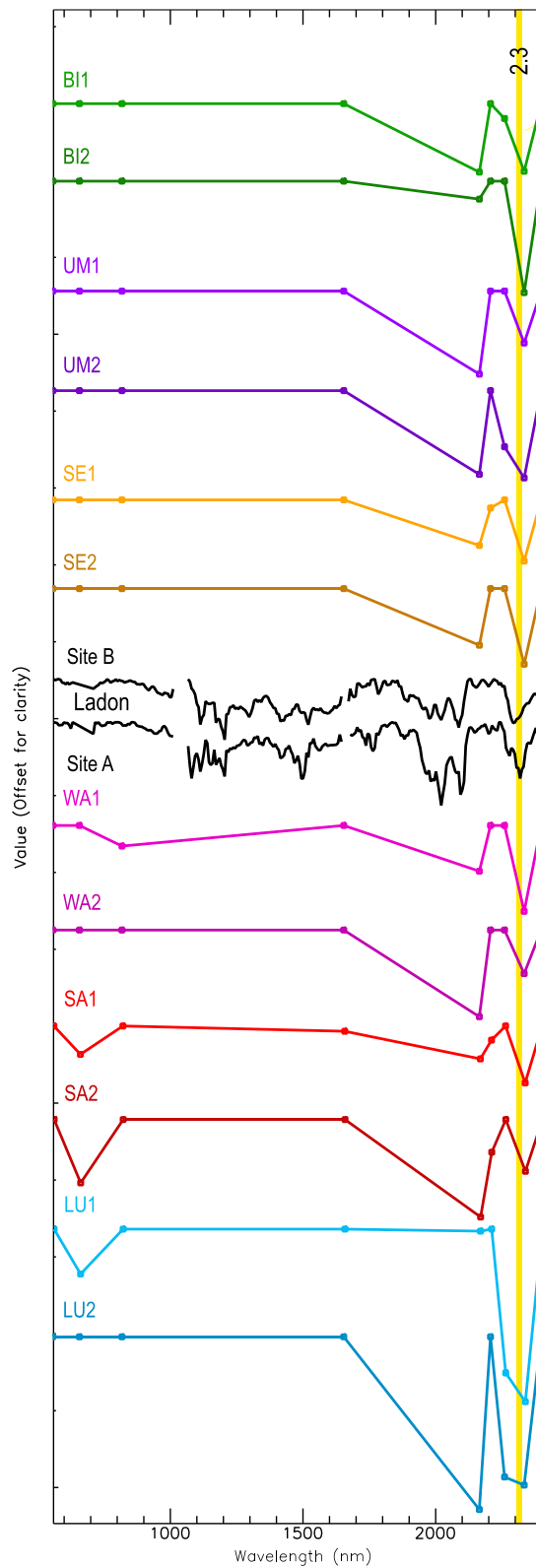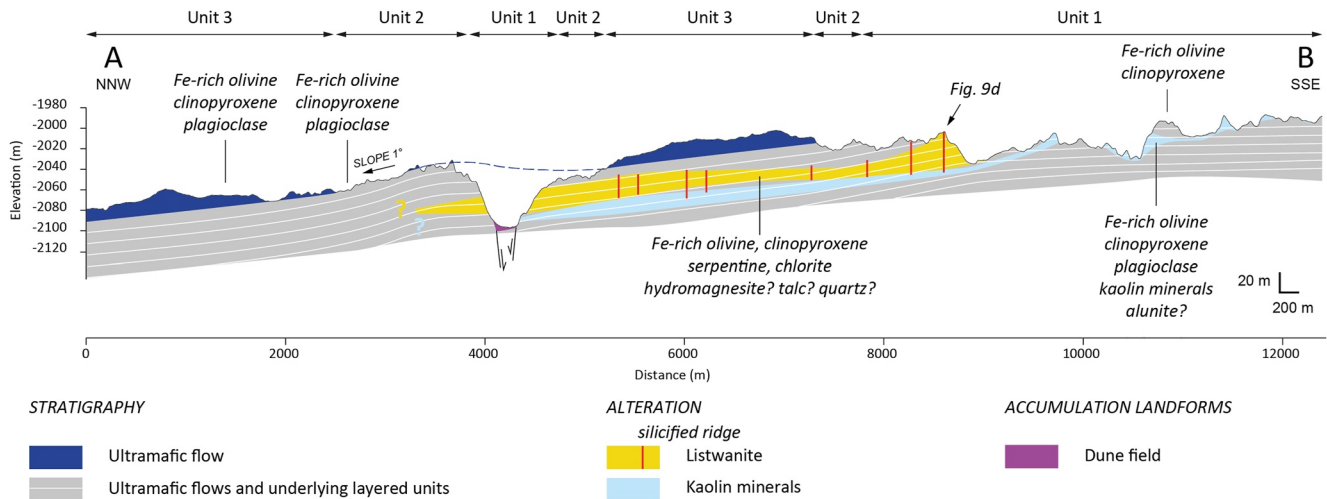
Figure 24.

Figure 25. Proposed geologic cross-section of the East Ladon study area. Location in Figure 5. Topography is from Context digital terrain model. Mineralogy is from CRISM data analysis. The location of the linear ridges (in red) is indicative.

- Unit 3 is cut by the Y-shaped graben, showing that the graben formed after Unit 3.
- The structural control of the silicified ridges by a stress field consistent with the formation of one of the Y-shaped graben branches suggests that from a mechanical perspective, hydrothermal alteration and graben formation were coeval.

From this analysis, the emplacement of Unit 3 in a shallow groundwater-bearing crust was coeval with hydrothermal activity and yellow-orange terrain alteration, with subaerial weathering of the warmed but cooler groundwater and white terrain formation and with graben opening. Figure 26 illustrates these mechanisms. Dating of Unit 3 (Figure 22a) indicates that these events occurred during the early Amazonian. Olivine and pyroxene from the rocks in which groundwater was circulating would be mobilized by hydrothermal activity, providing iron, magnesium, calcium, and silica required for serpentinization and listwanitization. Plagioclase would also contribute, but being a source of calcium and aluminum too, its dissolution would be a key to the formation of kaolin minerals. Plagioclase subaerial weathering, as well as carbonate formation in the listwanite, requires acidic water and therefore dissolved CO_2 in the H_2O groundwater reservoir. The contribution of atmosphere to the CO_2 and H_2O supply would have been fostered by rainfall (e.g., Weitz et al., 2022), but interactions with the subsurface would have been hampered by the flowing or cooling sheet of ultramafic composition.

6.9. Comparison With Other Serpentine Detections on Mars

Serpentinization has been reported at several places in a diversity of environments, including Nili Fossae, Syrtis Major, along the Claritas Rise—Thaumasia highlands—Coprates Rise arc south of Valles Marineris, in crater ejecta and central peaks (Brown et al., 2010; Ehlmann et al., 2009, 2010, 2011; Viviano-Beck et al., 2017; Viviano et al., 2013), and between the Hellas and Isidis basins (Bultel et al., 2015).

In these works, serpentinite detections have been commonly reported to be associated with carbonates, and sometimes chlorite and talc. Several differences exist, however, with the geologic environment of our study area in East Ladon. These works found that serpentinization and carbonation occurred between the pre-Noachian and early Hesperian; smectites were commonly found to be associated with the serpentines and carbonates, as well as low-grade metamorphic minerals (such as zeolites, prehnite); the correlation with tectonic events was loose. The mineral assemblages found by Brown et al. (2010) and Viviano et al. (2013) are the closest to those identified

Figure 24. Comparison between the Compact Reconnaissance Imaging Spectrometer for Mars spectra at Sites A and B, representative of the yellow-orange terrain, and ASTER spectra of samples of six listwanite ridges (BI1, BI2: Bir Umq ophiolite, Arabia; LU1, LU2: Luobusa, Tsangpo suture, Tibet; SA1, SA2: Sartohay ophiolite, West Junggar suture; SE1, SE2: Semail ophiolite, Oman; UM1, UM2: Um Khalisa ophiolite, Eastern Desert, Egypt; and WA1, WA2: Wadi Abu Fas ophiolite, South Eastern Desert, Egypt). The continuum between 0.560 and 2.400 μm was removed. The coordinates of the ASTER pixels are given in Section 4 in Supporting Information S1.
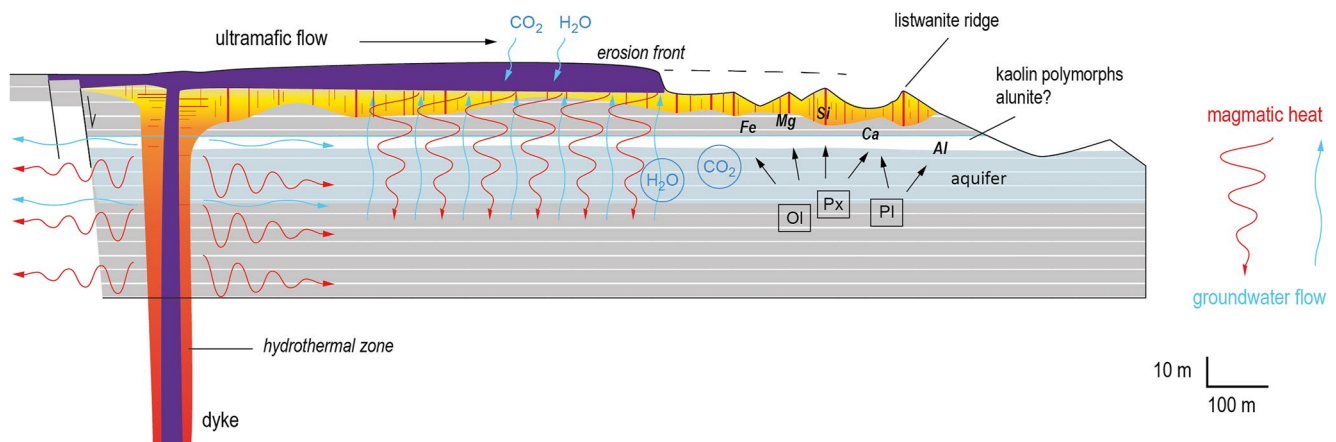
Figure 26. Elements for a volcanic-hydrological model of mineral formation in East Ladon in relation to its extensional tectonic setting. In this model, Unit 3 is fed by a dike. All the minerals identified in the CRISM cube, and probably some undetected, form in response to the emplacement of the Unit 3 ultramafic volcanic flow. The heat gradient, which increases upward, generates high pressurization at the top of the aquifer, resulting in serpentinization and listwanitization (yellow-orange terrain, silicified ridges). At a lower level, lower temperature, and lower water pressurization, kaolin polymorphs form by the dissolution of plagioclase (white terrain). Modulated by the local forming conditions, halloysite would form low in the aquifer (lower temperature), kaolinite at a shallower depth, then dickite at the highest level and already in the hydrothermal environment. Due to the metastability of halloysite and dickite, kaolinite might be the main mineral remaining today. The yellow-orange and white terrains are exhumed by erosion of Unit 3. Aquifer depth is unconstrained.

here. None of these works, however, reported any association between these minerals and linear ridges similar to those found in East Ladon.

7. Conclusion

In the past, most of the Ladon basin infilling has been interpreted as sedimentary deposits, such as aqueous sediments, evaporites, or duricrust (Irwin & Grant, 2013). However, Irwin and Grant (2013) did not exclude the presence of volcanic sheets interbedded within the sedimentary sequence and more probably in the upper part of the succession. The high effectiveness of color composite CaSSIS data together with the general framework given by CTX mosaics, the detailed stratigraphic relationship revealed by HiRISE data and the compositional information obtained from spectral analyses on CRISM data allowed us to shed light on the later geological evolution of the basin, in which syntectonic upper Hesperian to lower Amazonian volcanic and hydrothermal activity plays a prominent role.

Listwanitization is reported here for the first time as a mechanism that potentially operated on Mars. This process satisfactorily accounts for the mineralogical, geomorphological, structural, and topographic diversity of the study area in East Ladon. Other listwanitized regions probably exist and shall be identified in further investigations, increasing the variety of potential hydrothermal targets on Mars for future missions (e.g., Schulze-Makuch et al., 2007).

Serpentinization is one of the most considered processes potentially involved in the emergence of life (e.g., Lang & Brazelton, 2020; Stamenković et al., 2019), as a major source of energy through the supply of hydrogen, through the genesis of methane, the release of other elements of abiogenic origin (Russell et al., 2010), and through the genesis of highly reducing and high-pH fluids during exothermic serpentinization-associated reactions (Schrenk et al., 2013).

Quesnel et al. (2009) and Chassefière et al. (2013, 2016) revealed the Noachian potential of serpentinization, providing conditions prone to the emergence of life at that time. In Ladon, serpentinization occurred much later, in a fully different context. A strong requirement for life to emerge is the duration and stability of favorable conditions. Serpentinization provides environments shielded from climate instabilities, which are thought to have been dramatic in the Martian past (Laskar et al., 2004). However, the situation of life in the early Amazonian is unknown and without better constraints on the duration of activation of the hydrothermal cells generated in the serpentine system in Ladon and the difficulty of abiogenic carbon accessibility to potential living organisms in serpentine systems (Lang & Brazelton, 2020; Proskurowski et al., 2008; Schrenk et al., 2013), the likelihood of Amazonian life in the Ladon basin is far from being demonstrated.

Overall, this work emphasizes the effectiveness of CaSSIS color image analysis in the geologic interpretation of the surface of Mars. With the similar ∼6 m pixel size, CTX topography derived from stereoscopic image processing was found to be well adapted to CaSSIS color image interpretation in areas where CaSSIS stereoscopic image pairs are not available. CaSSIS has a huge potential for mapping the differences in the composition of large surface areas. It was shown to be helpful in identifying primary rocks versus alteration products with the capability of separating ferrous from ferric iron. Furthermore, the narrow ridges identified in the Ladon sites, also not identified before, had been identified using HiRISE images only; however, without the much broader coverage of the CaSSIS color images, which highlights their huge distribution, their resistance to erosion, and their unusual yellow-orange color, their significance as revealed in this study would have been much more difficult to find. The CaSSIS images provide a comfortable framework for the interpretation of CRISM data, and, having channels overlapping the HiRISE color channels, expand the HiRISE capabilities to larger surface areas and enhance scientific return.

Data Availability Statement

CRISM TER, CRISM MTRDR, CTX, and HiRISE RDR data are available in the NASA Planetary Data System (A. McEwen, 2007; Malin, 2007; Seelos, 2016a, 2016b, respectively). The CaSSIS calibrated data (https://doi.org/10.5270/esa-da0ic0t) are available in the ESA Planetary Science Archive. The splib07a, RELAB, and MICA spectral libraries are, respectively, available at USGS (Kokaly et al., 2017), in the NASA Planetary Data System (R. Milliken, 2019) and from Viviano-Beck et al. (2014). The ASTER L2 Surface Reflectance VNIR and Crosstalk Corrected SWIR V003 data are available at NASA EOSDIS Land Processes DAAC (NASA/METI/AIST/Japan Space Systems and U.S./Japan ASTER Science Team, 2001).

References

Ash, C. H. (2001). Relationship between ophiolites and gold-quartz veins in the North American Cordillera. *British Columbia Ministry of Energy and Mines, Bulletin*, *108*, 140.

Ash, C. H., & Arksley, R. L. (1990). The Atlin ultramafic allochthon: Ophiolitic basement within the Cache Creek terrane; tectonic and metallogenic significance. *British Columbia Ministry of Energy and Mines, Geological Survey Branch, Geological Fieldwork 1989, Paper 1990-1*, 365–374.

Azer, M. K. (2013). Evolution and economic significance of listwaenites associated with Neoproterozoic ophiolites in South Eastern Desert, Egypt. *Geológica Acta*, *11*(1), 113–128. https://doi.org/10.1344/105.000001777

Bamberg, M., Jaumann, R., Asche, H., Kneissl, T., & Michael, G. G. (2014). Floor-fractured craters on Mars – Observations and origin. *Planetary and Space Science*, *98*, 146–162. https://doi.org/10.1016/j.pss.2013.09.017

Bandfield, J. L., Glotch, T. D., & Christensen, P. R. (2003). Spectroscopic identification of carbonate minerals in the Martian dust. *Science*, *301*(5636), 1084–1087. https://doi.org/10.1126/science.1088054

Bauluz, B. (2015). Halloysite and kaolinite: Two clay minerals with geological and technological importance. *Revista de la Real Academia de Ciencias, Zaragoza*, *70*, 1–33. https://doi.org/10.1016/j.cretres.2014.03.014

Bishop, J. L., Dyar, M. D., Sklute, E. C., & Drief, A. (2008). Physical alteration of antigorite: A Mössbauer spectroscopy, reflectance spectroscopy and TEM study with applications to Mars. *Clay Minerals*, *43*(1), 55–67. https://doi.org/10.1180/claymin.2008.043.1.04

Bishop, J. L., Lane, M. D., Dyar, M. D., & Brown, A. J. (2008). Reflectance and emission spectroscopy study of four groups of phyllosilicates: Smectites, kaolinite-serpentines, chlorites and micas. *Clay Minerals*, *43*(1), 35–54. https://doi.org/10.1180/claymin.2008.043.1.03

Bishop, J. L., Murad, E., & Dyar, M. D. (2002). The influence of octahedral and tetrahedral cation substitution on the structure of smectites and serpentines as observed through infrared spectroscopy. *Clay Minerals*, *37*(4), 617–628. https://doi.org/10.1180/0009855023740064

Brown, A. J., Hook, S. J., Baldridge, A. M., Crowley, J. K., Bridges, N. T., Thomson, B. J., et al. (2010). Hydrothermal formation of clay-carbonate alteration assemblages in the Nili Fossae region of Mars. *Earth and Planetary Science Letters*, *297*(1–2), 174–182. https://doi.org/10.1016/j.epsl.2010.06.018

Brož, P., Krýza, O., Wilson, L., Conway, S., Hauber, E., Mazzini, A., et al. (2020). Experimental evidence for lava-like mud flows under Martian surface conditions. *Nature Geoscience*, *13*(6), 403–407. https://doi.org/10.1038/s41561-020-0577-2

Buckman, S., & Ashley, P. (2010). Silica-carbonate (listwanites) related gold mineralisation associated with epithermal alteration of serpentinite bodies. In *New England Orogen, 2010* (Vol. 94–105). University of New England.

Bultel, B., Quantin-Nataf, C., Andréani, M., Clénet, H., & Lozac'h, L. (2015). Deep alteration between Hellas and Isidis basins. *Icarus*, *260*, 141–160. https://doi.org/10.1016/j.icarus.2015.06.037

Caliński, T., & Harabasz, J. (1974). A dendrite method for cluster analysis. *Communications in Statistics*, *3*, 1–27. https://doi.org/10.1080/03610927408827101

Carr, M. H., & Head, J. W. (2015). Martian surface/near-surface water inventory: Sources, sinks, and changes with time. *Geophysical Research Letters*, *42*(3), 726–732. https://doi.org/10.1002/2014GL062464

Carr, M. H., & Head, J. W. (2019). Mars: Formation and fate of a frozen Hesperian ocean. *Icarus*, *319*, 433–443. https://doi.org/10.1016/j.icarus.2018.08.021

Casey, W. H., Westrich, H. R., & Holdren, G. R. (1991). Dissolution rate of plagioclase at pH = 2 and 3. *American Mineralogist*, *76*, 211–217.

Catling, D. C., & Zahnle, K. J. (2020). The Archean atmosphere. *Science Advances*, *6*(9), eaax1420. https://doi.org/10.1126/sciadv.aax1420

Chassefière, E., Langlais, B., Quesnel, Y., & Leblanc, F. (2013). The fate of early Mars' lost water: The role of serpentinization. *Journal of Geophysical Research: Planets*, *118*(5), 1123–1134. https://doi.org/10.1002/jgre.20089

Chassefière, E., Lasue, J., Langlais, B., & Quesnel, Y. (2016). Early Mars serpentinization-derived CH_4 reservoirs, H_2-induced warming and paleopressure evolution. *Meteoritics & Planetary Sciences*, *51*(11), 2234–2245. https://doi.org/10.1111/maps.12784

Choe, H., Mège, D., & Dyment, J. (2021). High-resolution magnetic investigation of hydrothermal circulation in the Danakil Depression. In *AGU Fall Meeting*. Abstract GP35C-033. Retrieved from https://agu.confex.com/agu/fm21/meetingapp.cgi/Paper/954649

Clark, R. N., King, T. V. V., Klejwa, M., Swayze, G. A., & Vergo, N. (1990). High spectral resolution reflectance spectroscopy of minerals. *Journal of Geophysical Research*, *95*(B8), 12653–12680. https://doi.org/10.1029/JB095iB08p12653

Cloutis, E. A., Grasby, S. E., Last, W. M., Léveillé, R., Osinski, G., & Sherriff, B. L. (2010). Spectral reflectance properties of carbonates from terrestrial analogue environments: Implications for Mars. *Planetary and Space Science*, *48*(4), 522–537. https://doi.org/10.1016/j.pss.2009.09.002

Collanega, L., Corti, G., Breda, A., Massironi, M., & Keir, D. (2020). 3D extension at plate boundaries accommodated by interacting fault systems. *Scientific Reports*, *10*(1), 8669. https://doi.org/10.1038/s41598-020-65599-5

De Ligny, D., & Navrotsky, A. (1999). Energetics of kaolin polymorphs. *American Mineralogist*, *84*(4), 506–516. https://doi.org/10.2138/am-1999-0404

Dickson, J. L., Kerber, L. A., Fassett, C. I., & Ehlmann, B. L. (2018). A global, blended CTX mosaic of Mars with vectorized seam mapping: A new mosaicking pipeline using principles of non-destructive image editing. In *Paper presented at the 49th Lunar and Planetary Science Conference*. Lunar and Planetary Institute. Abstract #2480.

Douté, S., & Jiang, C. (2019). Small-scale topographical characterization of the Martian surface with in-orbit imagery. *IEEE Transactions on Geoscience and Remote Sensing*, *58*(1), 447–460. https://doi.org/10.1109/TGRS.2019.2937172

Dyar, M. D., Sklute, E. C., Menzies, O. N., Bland, P. A., Lindsley, D., Glotch, T., et al. (2009). Spectroscopic characteristics of synthetic olivine: An integrated multi-wavelength and multi-technique approach. *American Mineralogist*, *94*(7), 883–898. https://doi.org/10.2138/am.2009.3115

Ece, Ö. I., Ekinci, B., Schroeder, P. A., Crowe, D., & Esenli, F. (2013). Origin of the Düvertepe kaolin–alunite deposits in Simav Graben, Turkey: Timing and styles of hydrothermal mineralization. *Journal of Volcanology and Geothermal Research*, *255*, 57–78. https://doi.org/10.1016/j.jvolgeores.2013.01.012

Ehlmann, B. L., Mustard, J. F., Clark, R. N., Swayze, G. A., & Murchie, S. L. (2011). Evidence for low-grade metamorphism, hydrothermal alteration, and diagenesis on Mars from phyllosilicate mineral assemblages. *Clays and Clay Minerals*, *59*(4), 359–377. https://doi.org/10.1346/CCMN.2011.0590402

Ehlmann, B. L., Mustard, J. F., & Murchie, S. L. (2010). Geologic setting of serpentine deposits on Mars. *Geophysical Research Letters*, *37*(6), L06201. https://doi.org/10.1029/2010GL042596

Ehlmann, B. L., Mustard, J. F., Murchie, S. L., Poulet, F., Bishop, J. L., Brown, A. J., et al. (2008). Orbital identification of carbonate-bearing rocks on Mars. *Science*, *322*(5909), 1828–1831. https://doi.org/10.1126/science.1164759

Ehlmann, B. L., Mustard, J. F., Swayze, G. A., Clark, R. N., Bishop, J. L., Poulet, F., et al. (2009). Identification of hydrated silicate minerals on Mars using MRO-CRISM: Geologic context near Nili Fossae and implications for aqueous alteration. *Journal of Geophysical Research*, *114*, E00D08. https://doi.org/10.1029/2009JE003339

European Space Agency. (2021). ExoMars 2016 CaSSIS calibrated data product collection, 2.2. https://doi.org/10.5270/esa-da0ic0t

Falk, E. S., & Kelemen, P. B. (2015). Geochemistry and petrology of listvenite in the Samail ophiolite, Sultanate of Oman: Complete carbonation of peridotite during ophiolite emplacement. *Geochimica et Cosmochimica Acta*, *160*, 70–90. https://doi.org/10.1016/j.gca.2015.03.014

Ferenc, Š., Uher, P., Spišiak, J., & Šimonová, V. (2016). Chromium- and nickel-rich micas and associated minerals in listvenite from the Muránska Zdychava, Slovakia: Products of hydrothermal metasomatic transformation of ultrabasic rock. *Journal of Geosciences*, *61*, 239–254. https://doi.org/10.3190/jgeosci.217

Gahlan, H. A., Azer, M. K., Asimow, P. D., & Kahtany, K. M. (2022). formation of gold-bearing listvenite in the mantle section of the Neoproterozoic Bir Umq ophiolite, Western Arabian Shield, Saudi Arabia. *Journal of African Earth Sciences*, *190*, 104517. https://doi.org/10.1016/j.jafrearsci.2022.104517

Grant, J. A., & Parker, T. J. (2002). Drainage evolution in the Margaritifer Sinus region, Mars. *Journal of Geophysical Research*, *107*(E9), 5066. https://doi.org/10.1029/2001JE001678

Gudmundsson, A., Fjeldskaar, I., & Brenner, S. L. (2002). Propagation pathways and fluid transport of hydrofractures in jointed and layered rocks in geothermal fields. *Journal of Volcanology and Geothermal Research*, *116*(3–4), 257–278. https://doi.org/10.1016/S0377-0273(02)00225-1

Gurgurewicz, J., Mège, D., Schmidt, F., Douté, S., & Langlais, B. (2022). Megashears and hydrothermalism at the Martian crustal dichotomy in Valles Marineris. *Communications Earth & Environment*, *3*(1), 282. https://doi.org/10.1038/s43247-022-00612-5

Hamdy, M. M., El Saeed, R. L., & Abdelwahab, W. (2022). Gold-bearing listwaenites in ophiolitic ultramafics from the Eastern Desert of Egypt: Subduction zone-related alteration of Neoproterozoic mantle? *Journal of African Earth Sciences*, *193*, 104574. https://doi.org/10.1016/j.jafrearsci.2022.104574

Hangx, S. J. T., & Spiers, C. J. (2009). Reaction of plagioclase feldspars with CO_2 under hydrothermal conditions. *Chemical Geology*, *265*(1–2), 88–98. https://doi.org/10.1016/j.chemgeo.2008.12.005

Hansen, L. D., Dipple, G. M., Gordon, T. M., & Kellett, D. A. (2005). Carbonated serpentinite (listwanite) at Atlin, British Columbia: A geological analogue to carbon dioxide sequestration. *The Canadian Mineralogist*, *43*(1), 225–239. https://doi.org/10.2113/gscanmin.43.1.225

Hargitai, H. I., & Gulick, V. C. (2018). Late Amazonian-aged channel and island systems locate east of Olympus Mons, Mars. In R. J. Soare, S. J. Conway, & S. M. Clifford (Eds.), *Dynamic Mars* (pp. 121–154). Elsevier. https://doi.org/10.1016/B978-0-12-813018-6.00004-2

Hartmann, W. K., & Daubar, I. J. (2017). Martian cratering 11. Utilizing decameter scale crater populations to study Martian history. *Meteoritics & Planetary Sciences*, *52*(3), 493–510. https://doi.org/10.1111/maps.12807

Huppert, H. E., & Sparks, R. S. J. (1985). Komatiites I: Eruption and flow. *Journal of Petrology*, *26*(3), 694–725. https://doi.org/10.1093/petrology/26.3.694

Irwin, R. P., III, & Grant, J. A. (2013). Geologic map of MTM −15027, −20027, −25027, and −25032 Quadrangles, Margaritifer Terra region of Mars. (U.S. Geological Survey Scientific Investigations Map 3209). Pamphlet 11 p., 1 sheet, scale 1:1,000,000. https://doi.org/10.3133/sim3209

Jiang, C., Douté, S., Luo, B., & Zhang, L. (2017). Fusion of photogrammetric and photoclinometric information for high resolution DEMs from Mars in-orbit imagery. *ISPRS Journal of Photogrammetry and Remote Sensing*, *130*, 418–430. https://doi.org/10.1016/j.isprsjprs.2017.06.010

Jozwiak, L. M., Head, J. W., & Wilson, L. (2014). Lunar floor-fractured craters as magmatic intrusions: Geometry, modes of emplacement, associated tectonic and volcanic features, and implications for gravity anomalies. *Icarus*, *248*, 424–447. https://doi.org/10.1016/j.icarus.2014.10.052

Kelemen, P. B., Matter, J., Streit, E. E., Rudge, J. F., Curry, W. B., & Blusztajn, J. (2011). Rates and mechanisms of mineral carbonation in peridotite: Natural processes and recipes for enhanced, in situ CO_2 capture and storage. *Annual Review of Earth and Planetary Sciences*, *39*(1), 545–576. https://doi.org/10.1146/annurev-earth-092010-152509

King, T. V., & Clark, R. N. (1989). Spectral characteristics of chlorites and Mg-serpentines using high-resolution reflectance spectroscopy. *Journal of Geophysical Research*, *94*(B10), 13997–14008. https://doi.org/10.1029/JB094iB10p13997

Kirk, R. L., Howington-Kraus, E., Rosiek, M. R., Anderson, J. A., Archinal, B. A., Becker, K. J., et al. (2008). Ultrahigh resolution topographic mapping of Mars with MRO HiRISE stereo images: Meter-scale slopes of candidate Phoenix landing sites. *Journal of Geophysical Research*, *113*, E00A24. https://doi.org/10.1029/2007JE003000

Kneissl, T., van Gasselt, S., & Neukum, G. (2011). Map-projection-independent crater size-frequency determination in GIS environments–New software tool for ArcGIS. *Planetary and Space Science*, *59*(11–12), 1243–1254. https://doi.org/10.1016/j.pss.2010.03.015

Kokaly, R. F., Clark, R. N., Swayze, G. A., Livo, K. E., Hoefen, T. M., Pearson, N. C., et al. (2017). *USGS spectral library version 7 (data series 1035), data series* (p. 61). U.S. Geological Survey. https://doi.org/10.3133/ds1035

Korenaga, J., Planavsky, N. J., & Evans, D. A. D. (2017). Global water cycle and the coevolution of the Earth's interior and surface environment. *Philosophical Transactions of the Royal Society, Series A*, *375*(2094), 20150393. https://doi.org/10.1098/rsta.2015.0393

Lang, S. Q., & Brazelton, W. J. (2020). Habitability of the marine serpentinite subsurface: A case study of the lost city hydrothermal field. *Philosophical Transactions of the Royal Society, Series A*, *378*(2165), 20180429. https://doi.org/10.1098/rsta.2018.0429

Langlais, B., Thébault, E., Houliez, A., Purucker, M. E., & Lillis, R. J. (2019). A new model of the crustal magnetic field of Mars using MGS and MAVEN. *Journal of Geophysical Research: Planets*, *124*(6), 1542–1569. https://doi.org/10.1029/2018JE005854

Laskar, J., Correia, A. C. M., Gastineau, M., Joutel, F., Levrard, B., & Robutel, P. (2004). Long term evolution and chaotic diffusion of the insolation quantities of Mars. *Icarus*, *170*(2), 343–364. https://doi.org/10.1016/j.icarus.2004.04.005

Lillis, R. J., Deighan, J., Fox, J. L., Bougher, S. W., Lee, Y., Combi, M. R., et al. (2017). Photochemical escape of oxygen from Mars: First results from MAVEN in situ data. *Journal of Geophysical Research: Space Physics*, *122*(3), 3815–3836. https://doi.org/10.1002/2016JA023525

Lucchetti, A., Pajola, M., Galluzzi, V., Giacomini, L., Carli, C., Cremonese, G., et al. (2018). Mercury hollows as remnants of original bedrock materials and devolatilization processes: A spectral clustering and geomorphological analysis. *Journal of Geophysical Research: Planets*, *123*(9), 2365–2379. https://doi.org/10.1029/2018JE005722

Lucchetti, A., Pajola, M., Poggiali, G., Semenzato, A., Munaretto, G., Cremonese, G., et al. (2021). Volatiles on mercury: The case of hollows and the pyroclastic vent of Tyagaraja crater. *Icarus*, *370*, 114694. https://doi.org/10.1016/j.icarus.2021.114694

Luzzi, E., Rossi, A. P., Massironi, M., Pozzobon, R., Corti, G., & Maestrelli, D. (2021). Caldera crater collapse as the trigger of chaos and fractured craters on the Moon and Mars. *Geophysical Research Letters*, *48*(11), e2021GL092436. https://doi.org/10.1029/2021GL092436

Malin, M. C. (2007). MRO Context Camera experiment data record level 0 v1.0 [Dataset]. NASA Planetary Data System. https://doi.org/10.17189/1520266

Malin, M. C., Bell, J. F., III, Cantor, B. A., Caplinger, M. A., Calvin, W. M., Clancy, R. T., et al. (2007). Context camera investigation on board the Mars Reconnaissance Orbiter. *Journal of Geophysical Research*, *112*(E5), E05S04. https://doi.org/10.1029/2006JE002808

Marra, W. A., Hauber, E., McLelland, S. J., Murphy, B. J., Parsons, D. R., Conway, S. J., et al. (2015). Pressurized groundwater outflow experiments and numerical modeling of outflow channels on Mars. *Journal of Geophysical Research: Planets*, *119*(12), 2668–2693. https://doi.org/10.1002/2014JE004701

Marzo, G. A., Roush, T. L., Blanco, A., Fonti, S., & Orofino, V. (2006). Cluster analysis of planetary remote sensing spectral data. *Journal of Geophysical Research*, *111*(E3), E03002. https://doi.org/10.1029/2005JE002532

Marzo, G. A., Roush, T. L., Blanco, A., Fonti, S., & Orofino, V. (2008). Statistical exploration and volume reduction of planetary remote sensing spectral data. *Journal of Geophysical Research*, *113*(E12), E12009. https://doi.org/10.1029/2008JE003219

Marzo, G. A., Roush, T. L., & Hogan, R. C. (2009). Automated classification of visible and infrared spectra using cluster analysis. *Journal of Geophysical Research*, *114*(E8), E08001. https://doi.org/10.1029/2008JE003250

McEwen, A. (2007). *Mars Reconnaissance Orbiter high resolution imaging science experiment, reduced data record, MRO-M-HIRISE-3-RDR-V1.0*. NASA Planetary Data System. https://doi.org/10.17189/1520303

McEwen, A. S., Eliason, E. M., Bergstrom, J. W., Bridges, N. T., Hansen, C. J., Delamere, W. A., et al. (2007). Mars Reconnaissance Orbiter's high resolution imaging science experiment (HiRISE). *Journal of Geophysical Research*, *112*(E5), E05S02. https://doi.org/10.1029/2005JE002605

Mège, D., & Gurgurewicz, J. (2016). The Ophir Chasma dyke Swarm: Description and implications for the Genesis of the Valles Marineris northern troughs. *Acta Geologica Sinica (English Edition)*, *90*(s1), 180–182. https://doi.org/10.1111/1755–6724.12960

Mège, D., & Korme, T. (2004). Fissure eruption of flood basalts from statistical analysis of dyke fracture length. *Journal of Volcanology and Geothermal Research*, *131*(1–2), 77–92. https://doi.org/10.1016/S0377–0273(03)00317–2

Michael, G. G., Kneissl, T., & Neesemann, A. (2016). Planetary surface dating from crater size-frequency distribution measurements: Poisson timing analysis. *Icarus*, *277*, 279–285. https://doi.org/10.1016/J.ICARUS.2016.05.019

Michael, G. G., & Neukum, G. (2010). Planetary surface dating from crater size–frequency distribution measurements: Partial resurfacing events and statistical age uncertainty. *Earth and Planetary Science Letters*, *294*(3–4), 223–229. https://doi.org/10.1016/j.epsl.2009.12.041

Michael, G. G., Platz, T., Kneissl, T., & Schmedemann, N. (2011). Planetary surface dating from crater size–frequency distribution measurements: Spatial randomness and clustering. *Icarus*, *218*(Issue 1), 169–177. https://doi.org/10.1016/j.icarus.2011.11.033

Milliken, R. (2019). RELAB reflectance spectra data collection. https://doi.org/10.17189/1519032

Milliken, R. E., Hiroi, T., & Patterson, W. (2016). The NASA reflectance experiment laboratory (RELAB) facility: Past, present, and future. In *Paper presented at the 47th Lunar and Planetary Science Conference*.

Moore, D. E., Lockner, D. A., Summers, R., Shengli, M., & Byerlee, J. D. (1996). Strength of chrysotile-serpentinite gouge under hydrothermal conditions: Can it explain a weak San Andreas fault? *Geology*, *24*(11), 1041–1044. https://doi.org/10.1130/0091-7613(1996)024<1041:SOCSGU>2.3.CO;2

Murchie, S., Arvidson, R., Bedini, P., Beisser, K., Bibring, J.-P., Bishop, J., et al. (2007). Compact Reconnaissance Imaging Spectrometer for Mars (CRISM) on Mars Reconnaissance Orbiter (MRO). *Journal of Geophysical Research*, *112*(E5), E05S03. https://doi.org/10.1029/2006JE002682

Murchie, S. L., Seelos, F. P., Hash, C. D., Humm, D. C., Malaret, E., McGovern, A., et al. (2009). Compact Reconnaissance Imaging Spectrometer for Mars investigation and data set from the Mars Reconnaissance Orbiter's primary science phase. *Journal of Geophysical Research*, *114*, E00D07. https://doi.org/10.1029/2009JE003344

NASA/METI/AIST/Japan Space Systems and U.S./Japan ASTER Science Team. (2001). *ASTER level 2 surface reflectance product*. NASA EOSDIS Land Processes DAAC. https://doi.org/10.5067/ASTER/AST_07.003

Pajola, M., Lucchetti, A., Semenzato, A., Poggiali, G., Munaretto, G., Galluzzi, V., et al. (2021). Lermontov crater on Mercury: Geology, morphology and spectral properties of the coexisting hollows and pyroclastic deposits. *Planetary and Space Science*, *195*, 105136. https://doi.org/10.1016/j.pss.2020.105136

Pajola, M., Roush, T., Dalle Ore, C., Marzo, G. A., & Simioni, E. (2018). Phobos MRO/CRISM visible and near-infrared (0.5–2.5 micron) spectral modeling. *Planetary and Space Science*, *154*, 63–71. https://doi.org/10.1016/j.pss.2018.02.016

Proskurowski, G., Lilley, M. D., Seewald, J. S., Früh-Green, G. L., Olson, E. J., Lupton, J. E., et al. (2008). Abiogenic hydrocarbon production at Lost City hydrothermal field. *Science*, *319*(5863), 604–607. https://doi.org/10.1126/science.1151194

Qiu, T., & Zhu, Y. (2015). Geology and geochemistry of listwaenite-related gold mineralization in the Sayi gold deposit, Xinjiang, NW China. *Ore Geology Reviews*, *70*, 61–79. https://doi.org/10.1016/j.oregeorev.2015.03.017

Quesnel, Y., Sotin, C., Langlais, B., Costin, S., Mandea, M., Gotttschalk, M., & Dyment, J. (2009). Serpentinization of the Martian crust during Noachian. *Earth and Planetary Science Letters*, *277*(1–2), 184–193. https://doi.org/10.1016/j.epsl.2008.10.012

Robinson, P. T., Malpas, J., Zhou, M.-F., Ash, C., Yang, J.-S., & Bai, W.-J. (2005). Geochemistry and origin of listwanites in the Sartohay and Luobusa ophiolites, China. *International Geology Review*, *47*(2), 177–202. https://doi.org/10.2747/0020-6814.47.2.177

Rodriguez, J. A. P., Platz, T., Gulick, V., Baker, V. R., Fairén, A. G., Kargel, J., et al. (2015). Did the Martian outflow channels mostly form during the Amazonian Period? *Icarus*, *257*, 387–395. https://doi.org/10.1016/j.icarus.2015.04.024

Russell, M. J., Hall, A. J., & Martin, W. (2010). Serpentinization as a source of energy at the origin of life. *Geobiology*, *8*(5), 355–371. https://doi.org/10.1111/j.1472-4669.2010.00249.x

Sato, H., Kurita, K., & Baratoux, D. (2010). The formation of floor-fractured craters in Xanthe Terra. *Icarus*, *207*(1), 248–264. https://doi.org/10.1016/j.icarus.2009.10.023

Schmidt, F., Way, M. J., Costard, F., Bouley, S., Séjourné, A., & Aleinov, I. (2022). Circumpolar ocean stability on Mars 3 Gy ago. *Proceedings of the National Academy of Sciences*, *119*(4), e2112930118. https://doi.org/10.1073/pnas.2112930118

Schrenk, M. O., Brazelton, W. J., & Lang, S. Q. (2013). Serpentinization, carbon, and deep life. *Reviews in Mineralogy and Geochemistry*, *75*(1), 575–606. https://doi.org/10.2138/rmg.2013.75.18

Schultz, R. A. (2000). Localization of bedding plane slip and backthrust faults above blind thrust faults: Keys to wrinkle ridge structure. *Journal of Geophysical Research*, *105*(E5), 12035–12052. https://doi.org/10.1029/1999JE001212

Schulze-Makuch, D., Dohm, J. M., Fan, C., Fairén, A. G., Rodriguez, J. A. P., Baker, V. R., & Fink, W. (2007). Exploration of hydrothermal targets on Mars. *Icarus*, *308*(2), 189–204. https://doi.org/10.1016/j.icarus.2007.02.007

Schumacher, S., & Zegers, T. E. (2011). Aram Chaos and its constraints on the surface heat flux of Mars. *Icarus*, *211*(1), 305–315. https://doi.org/10.1016/j.icarus.2010.09.023

Seelos, F. (2016a). *Mars Reconnaissance Orbiter Compact Reconnaissance Imaging Spectrometer for Mars Map-projected Targeted Reduced Data Record, MRO-M-CRISM-5-RDR-MPTARGETED-V1.0*. NASA Planetary Data System. https://doi.org/10.17189/1519470

Seelos, F. (2016b). *Mars Reconnaissance Orbiter Compact Reconnaissance Imaging Spectrometer for Mars Targeted Empirical Record, MRO-M-CRISM-4-RDR-TARGETED-V1.0*. NASA Planetary Data System. https://doi.org/10.17189/1519573

Sherlock, R. L., & Logan, M. A. V. (1995). Silica-carbonate alteration of serpentinite: Implications for the association of mercury and gold mineralization in Northern California. *Exploration And Mining Geology*, *4*(4), 395–409.

Stamenković, V., Beegle, L. W., Zacny, K., Arumugam, D. D., Baglioni, P., Barba, N., et al. (2019). The next Frontier for planetary and human exploration. *Nature Astronomy*, *3*(2), 116–120. https://doi.org/10.1038/s41550-018-0676-9

Stanger, G. (1985). Silicified serpentinite in the Semail nappe of Oman. *Lithos*, *18*, 13–22. https://doi.org/10.1016/0024-4937(85)90003-9

Stone, S. W., Yelle, R. V., Benna, M., Lo, D. Y., Elrod, M. K., & Mahaffy, P. R. (2020). Hydrogen escape from Mars is driven by seasonal and dust storm transport of water. *Science*, *370*(6518), 824–831. https://doi.org/10.1126/science.aba5229

Szitkar, F., Dyment, J., Choi, Y., & Fouquet, Y. (2014). What causes low magnetization at basalt-hosted hydrothermal sites? Insights from inactive site Krasnov (MAR 16°38'N). *Geochemistry, Geophysics, Geosystems*, *15*(4), 1441–1451. https://doi.org/10.1002/2014GC005284

Szitkar, F., Dyment, J., Fouquet, Y., Honsho, C., & Horen, H. (2014). The magnetic signature of ultramafic-hosted hydrothermal sites. *Geology*, *42*(8), 715–518. https://doi.org/10.1130/G35729.1

Templeton, A. S., & Ellison, E. T. (2020). Formation and loss of metastable brucite: Does Fe(II)-bearing brucite support microbial activity in serpentinizing ecosystems? *Philosophical transactions of the Royal Society, Series A*, *378*(2165), 20180423. https://doi.org/10.1098/rsta.2018.0423

Thomas, N., Cremonese, G., Ziethe, R., Gerber, M., Brändli, M., Bruno, G., et al. (2017). The colour and stereo surface imaging system (CaSSIS) for the ExoMars trace gas orbiter. *Space Science Reviews*, *212*(3–4), 1897–1944. https://doi.org/10.1007/s11214-017-0421-1

Thomas, N., Pommerol, A., Almeida, M., Read, M., Cremonese, G., Simioni, E., et al. (2022). Absolute calibration of the colour and stereo surface imaging system (CaSSIS). *Planetary and Space Science*, *211*, 105394. https://doi.org/10.1016/j.pss.2021.105394

Tominaga, M., Beinlich, A., Lima, E. A., Tivey, M. A., Hampton, B. A., Weiss, B., & Harigane, Y. (2017). Multi-scale magnetic mapping of serpentinite carbonation. *Nature Communications*, *8*(1), 1870. https://doi.org/10.1038/s41467-017-01610-4

Torson, J. M., & Becker, K. J. (1997). ISIS—A software Architecture for processing planetary images. In *Paper presented at Lunar and Planetary Science Conference XXVIII* (p. 443).

Ulrich, M., Muñoz, M., Guillot, S., Cathelineau, M., Picard, C., Quesnel, B., et al. (2014). Dissolution–precipitation processes governing the carbonation and silicification of the serpentinite sole of the New Caledonia ophiolite. *Contributions to Mineralogy and Petrology*, *167*(1), 952. https://doi.org/10.1007/s00410-013-0952-8

Vincendon, M. (2013). Mars surface phase function constrained by orbital observations. *Planetary and Space Science*, *76*, 87–95. https://doi.org/10.1016/j.pss.2012.12.005

Viviano-Beck, C. E., Murchie, S. L., Beck, A. W., & Dohm, J. M. (2017). Compositional and structural constraints on the geologic history of eastern Tharsis Rise, Mars. *Icarus*, *284*, 43–58. https://doi.org/10.1016/j.icarus.2016.09.005

Viviano-Beck, C. E., Seelos, F. P., Murchie, S. L., Kahn, E. G., Seelos, K. D., Taylor, H. W., et al. (2014). Revised CRISM spectral parameters and summary products based on the currently detected mineral diversity on Mars. *Journal of Geophysical Research: Planets*, *119*(6), 1403–1431. https://doi.org/10.1002/2014JE004627

Viviano, C. E., Moersch, J. E., & McSween, H. Y. (2013). Implications for early hydrothermal environments on Mars through the spectral discrimination of carbonation and chloritization reactions in the Nili Fosse region. *Journal of Geophysical Research: Planets*, *118*(9), 1858–1872. https://doi.org/10.1002/jgre.2014

Warner, N. H., Gupta, S., Calef, F., Grindrod, P., Boll, N., & Goddard, K. (2015). Minimum effective area for high resolution crater counting of Martian terrains. *Icarus*, *245*, 198–240. https://doi.org/10.1016/j.icarus.2014.09.024

Wawersik, W. R., Rudnicki, J. W., Dove, P., Harris, J., Logan, J. M., Pyrak-Nolte, L., et al. (2001). Terrestrial sequestration of CO_2: An assessment of research needs. *Advances in Geophysics*, *43*, 97–177. https://doi.org/10.1016/S0065-2687(01)80003-0

Weitz, C. M., Bishop, J. L., Grant, J. A., Wilson, S. A., Irwin, R. P., III, Saranathan, A. M., et al. (2022). Clay sediments derived from fluvial activity in and around Ladon basin, Mars. *Icarus*, *384*, 115090. https://doi.org/10.1016/j.icarus.2022.115090

Wenner, D. B., & Taylor, H. P. (1971). Temperatures of serpentinization of ultramafic rocks based on O^{18}/O^{16} fractionation between coexisting serpentine and magnetite. *Contributions to Mineralogy and Petrology*, *32*(3), 165–185. https://doi.org/10.1007/bf00643332

Wray, J. J., Murchie, S. L., Bishop, J. L., Ehlmann, B. L., Milliken, R. E., Wilhelm, M. B., et al. (2016). Orbital evidence for more widespread carbonate-bearing rocks on Mars. *Journal of Geophysical Research: Planets*, *121*(4), 652–677. https://doi.org/10.1002/2015JE004972

Xiangzhen, X., Jingsui, Y., Songyong, C., Qingsong, F., Wenji, B., & Dengzhu, B. (2009). Unusual mantle mineral group from chromitite orebody Cr-11 in Luobusa ophiolite of Yarlung-Zangbo suture zone, Tibet. *Journal of Earth Sciences*, *20*(2), 284–302. https://doi.org/10.1007/s12583-009-0026-z

Zhang, H., Gilbert, B., & Banfield, J. F. (2021). Atomic perspective on the serpentine–chlorite solid-state transformation. *Chemistry of Materials*, *33*(16), 6338–6345. https://doi.org/10.1021/acs.chemmater.1c00894

Zhang, L., Yang, J., Robinson, P. T., Xiong, F., Chen, Y., Lai, S., & Chen, M. (2015). Origin of listwanite in the Luobusa ophiolite, Tibet, implications for chromite stability in hydrothermal systems. *Acta Geologica Sinica*, *89*(2), 402–417. https://doi.org/10.1111/1755-6724.12438

Zotov, A., Mukhamet-Galeev, A., & Schott, J. (1998). An experimental study of kaolinite and dickite relative stability at 150–300°C and the thermodynamic properties of dickite. *American Mineralogist*, *83*(5–6), 516–524. https://doi.org/10.2138/am-1998-5-610

References From the Supporting Information

Carter, J., Poulet, F., Murchie, S. L., & Bibring, J.-P. (2013). Automated processing of planetary hyperspectral datasets for the extraction of weak mineral signatures and applications to CRISM observations of hydrated silicates on Mars. *Planetary and Space Science*, *76*, 53–67. https://doi.org/10.1016/j.pss.2012.11.007